Effects of Internal Structure of Porous Primitive Bodies on Their Impact Processes

Machii, Nagisa

(Degree)
博士（理学）

(Date of Degree)
2012-03-25

(Date of Publication)
2013-06-26

(Resource Type)
doctoral thesis

(Report Number)
甲5587

(URL)
https://hdl.handle.net/20.500.14094/D1005587

博士論文

Effects of Internal Structure of Porous Primitive Bodies on Their Impact Processes

(空隙を含む始原天体の内部構造が
衝突過程に与える影響)

平成24年1月
神戸大学理学研究科

町井　渚
NAGISA MACHII

Doctoral Dissertation

Effects of Internal Structure of Porous Primitive Bodies on Their Impact Processes

January, 2012

Graduate School of Science,
Kobe University

NAGISA MACHII

Contents

Abstract

Porous small bodies in the solar system were found by ground based observations and space exploration. It is presumed that these bodies have a variety of internal structure. Experiments are performed for a body which has large gaps between components reaccumulated after impact disruption, which has many voids due to evaporation of volatile component and which has numerous voids according to coalescence of fine dust. The strength of the body depends on its internal structure. Thus the internal structure of porous bodies has a major effect on impact outcome.

In this study, I conducted experimental studies on two topics for porous bodies consisting of multiple components. First is the relation between the bulk strength of sintered porous bodies and specific energy density for impact disruption (Q^*_s), especially for bodies having different size ratio of component and target (Relative Component Size, RCS). Second is the relation between the bulk strength of agglomerates and the transition velocity of bouncing-intrusion for a projectile impacting into the agglomerates. The former study simulates impact disruption of icy bodies consist of multiple components such as Kuiper belt objects and Saturnian small satellites. The latter simulates a possible formation process of the parent bodies of chondrites by chondrules being embedded into matrix.

In Chapter 1, an introduction is presented about the function of impact in the solar system and the physical processes of impact between small bodies. Q^*_s, important parameter on impact disruption of small bodies, is described in detail. The relation between the impact disruption and the bulk strength and porosity of the bodies, and the fundamental formulas for impact are described.

In Chapter 2, the study on the effects of the change of bulk strength due to sintering and RCS on Q^*_s are explained. Sintering is defined a process of making connection between components below the melting

point. Sintering is likely to occur for material such as water ice depending on location in outer space. The bulk strength of a body is expected to be strengthen by the physical connection between the components due to sintering.

At first, bulk strength of sintered equal-sized dimer was investigated. Samples used in the experiments were glass bead with rough surface of 4.9 mm in diameter and glass bead with smooth surface of 4.7 mm in diameter. They were heated for 0.5 to 240 hours under 32 patterns at 570, 600 and 630 °C. The size of the connecting part, called neck, was measured by the images taken by a microscope. Tensile and bending strength of sintered dimer were measured. Difference of surface roughness didn't appear when neck radius is much larger than 0.4 mm. The critical tensile force to break a neck is proportional to the square of neck radius, that is cross section of the neck only when the neck radius is much larger than 0.4 mm. The critical bending force to break a neck is proportional to the cube of the neck radius. The bending force is comparable to the tensile force when neck radius is large enough, although the bending force is smaller than the tensile force at smaller neck radius.

Based on the result of physical properties of sintered dimers, the bulk strength of sintered agglomerates were examined. Sample used in the experiment was the glass bead with smooth surface of 4.7 mm in diameter. The agglomerates consist of 90 particles. They have a three-layered-structure and each layer consists of 30 particles. Sintered agglomerates with two different bulk strengths were formed by baking the beads for 8 and 20 hours at 630 °C. The tensile strength obtained by Brazilian disc test for the two types of sintered agglomerates was 3.53×10^5 and 7.4×10^5 Pa, respectively. It was found that the specific tensile force to break the agglomerates, which was the applied force on the fractured cross-section divided by the number of broken necks, is comparable to the force for the dimers.

Impact disruption experiments were performed for these two types of sintered agglomerates. Projectiles were cylindrical polycarbonate of 3 mm in diameter, 6 mm in length and soda-lime glass sphere of about 3 mm in diameter. A projectile impacted into a target at impact velocity from 37 to 280 m/s using a helium gas-gun installed at Kobe University. Q_s^* for the targets are 4.7 and 10.6 J/kg, respectively. As the result, stronger target has larger Q_s^*.

The effect of RCS on Q_s^* was then examined. Targets of 20-hour and 8-hour sintering were called typeA and typeB. Both of targets have RCS of 0.19. Their Q_s^* is one order smaller than the previous studies for

the targets with the similar tensile strength and the much smaller RCS ($\sim 10^{-3}$). Sintered agglomerates of 30 mm in diameter and 12 mm in height with smaller RCS were formed using glass beads of 0.73 mm in average diameter. Their tensile strength was 2.9×10^5. This target is called typeC. Q_s^* of typeC was 44.2 J/kg and is comparable to the previous targets with RCS of 10^{-3}. These results are probably due to much smaller number of necks for the stress wave to travel through the agglomerates and therefore the energy dissipation at the necks is minimal. Also, the much larger fraction of the surface particles enables the particles to move more freely and thus be broken more easily. These are the reasons why that sintered agglomerates with larger RCS have smaller Q_s^* and were broken easily. It implies that sintered icy bodies have a range of Q_s^* depending on RCS.

In Chapter 3, the study on the relation between the impact pressure and the strength of porous body is described. Chondrites is one of major groups of meteorite. Chondrites consist of spherical objects called chondrules which are glassy and typically millimeter-sized and fine grains called matrix. It was found from previous analyses that chondrules were molten under high temperature environment and rapidly cooled down. The common point of three major models for chondrule formation is that chondrules were formed at local place in protoplanetary disk. In this study, I assumed that chondrules and matrix were formed at different places in the protoplanetary disk and subsequently they collided each other. The size of matrix is at least larger than a few cm at 1000 years after CAI formation according to the standard model of the solar system formation. I investigated the threshold velocity for a chondrule being embedded into matrix and the minimum size for matrix to capture a chondrule.

Sample used in the experiment was polydisperse spherical silica particles of 0.8 μm in diameter as matrix analog. Collision experiments were performed using three accelerators depending on collision velocities. Impact experiments at low velocity (from 0.2 to 2 m/s) were performed using a drop tube of 20 cm in inner diameter and about 2 m in length installed at TU Braunschweig, Germany. The projectiles were glass beads of 1 and 4.7 mm in diameter as chondrule analogs and the targets were porous dust aggregates of 50, 75 and 90 % in porosity as matrix analog. For impact experiments at medium velocity (from 2 to 5 m/s) and high velocity (from 20 to 300 m/s), a spring gun and a helium gas-gun at Kobe University were used, respectively. The projectiles were glass beads of 1 and 3 mm in diameter and the targets were porous dust aggregates of 50 and 75 % in porosity.

Static strength measurements for silica agglomerates were performed to investigate the mechanical properties. Silica particles were poured into cylindrical stainless container of 5, 10, 15 and 20 mm in inner diameter and compressed up to 9.8 kN at 0.01 mm/s using a compressive strength testing machine in order to measure the compression (pressure-porosity) curve. The elastic limits of the dust agglomerate were also determined.

There were three types of collisional outcomes; bouncing, (nearly) sticking and intrusion of the projectile. It was indicated that intrusion occurs for a target with higher porosity or at higher impact velocity. The relation between the impact pressure and the static strength of porous targets were discussed as follows. Impact pressure was given by the density and the sound velocity of the target and the impact velocity. The sound velocities of the targets were derived from the slope of compression curve within the elastic limit and were 460, 15 and 2 m/s for 50, 75 and 90 % porosity targets. The elastic limit pressure, that is the compressive strength of the dust agglomerate was found to be comparable to the values on the compression curves of dust agglomerates. Thus we assumed the compressive strength of target with certain porosity is able to be estimate from the point on the compression curve. Comparing the compressive strength of the target with the impact pressure, it was found that intrusion occurs when the strength of the target is smaller than the impact pressure. Meanwhile bouncing occurs when the strength of the target is larger than the impact pressure.

The critical intrusion velocities of the targets with 50 and 75 % in porosity were determined to 46 and 3 m/s, respectively. If a projectile of 3 mm in diameter has relative velocity of 46 or 3 m/s, a target has 90 or 10 cm in diameter in protoplanetary disk according to a model of planetary formation. The estimated aggregate sizes by the model is larger than the experimental results of 3 cm and < 7.5 mm and then enough to capture a projectile.

In Chapter 4, I summarized these two studies. It was found that the bodies which has the same static bulk strength may have different Q_s^* depending on the internal structure such as RCS. Whether the collision outcome is intrusion or bouncing can be estimated by a comparison of the bulk strength of the target and the impact pressure.

Chapter 1

General introduction

1.1 Impact processes in the solar system

Our solar system consists of one star, eight planets and their moons, and numerous small solar system bodies such as asteroids, trans-Neptunian objects, and comets. From the early stage of the solar system, many objects have experienced some sort of impacts or collisions and evolved into their present shapes.

Impacts or collisions can be classified three different categories depending on outcome: cratering, shattering, and dispersing. There is much evidence that planets, asteroids, and the other small objects in the solar system have undergone impact or collision. The first category is defined by events leading to the formation of craters accompanied by ejection of material but without affecting the physical integrity of the main body. For example, there are numerous craters on the surface of the Moon. A crater is formed by the impact of the small object. These craters have been seen on the surface of Earth, Mars, Mercury, satellites, and larger asteroids (e.g., 243 Ida). These bodies have undergone multiple impacts in their evolutionary history.

Shattering impacts are events that break the parent body into smaller pieces. After shattering, reaccretion occurs if ejection velocities of smaller pieces are slower than escape velocity of the parent body. Reaccreted agglomerate has gaps between component pieces. Because of these gaps, reaccreted body has smaller density than before and bulk strength of the body is weaker. This internal structure of the body

is called a "rubble-pile" structure. Rubble-pile asteroids have higher bulk porosity than the monolithic ones. Britt *et al.* (2002) estimated bulk porosity of asteroids using their bulk density. The density of the asteroid was scaled by the density of the meteoritic analog which has the similar reflectance spectrum as the asteroid. Several asteroids were classified as rubble-pile (e. g., 16 Psyche, 22 Kalliope, 45 Eugenia, 90 Antiope, 253 Mathilde). Rubble-pile objects have a smaller size (< 200 km) with irregular shapes due to lack of self gravity (Sheppard and Jewitt, 2002). There are no clear craters on the surface of 25143 Itokawa. This may be because its surface consists of large sized components, e.g., boulders and pebbles (Hirata *et al.*, 2009).

Dispersing events are those which not only break the bodies into pieces, but also manage to accelerate velocities of those fragments to exceed the escape velocity. One observational evidence is asteroid families such as Koronis. A meteorite is the object which fell down and could survive the impact with the Earth's surface. These meteorites are formed as the result of impact. Different from the shattering event, broken small pieces after impact have high velocity enough to exceed the escape velocity of their parent bodies. Another case for result of dispersing is ejecta from cratering impact. For example, Martian meteorites come from Mars. Small fragments eject from the Martian surface and reach the Earth's surface.

As described above, the evidence is obvious when the bodies have impacted or collided from their surface, internal structure and orbit. In the history of the solar system, impact or collision plays a trigger in the progress of the their evolution.

1.2 Important parameters for small bodies' impact processes

1.2.1 Classification of impact outcomes

As described above, there are three different categories in impact or collision outcomes: cratering, shattering, and dispersing. Depending on body size, there are two regimes, strength and gravity regime. In the strength regime, the outcomes of the impacts are dominated by their strength. In the gravity regime, the outcomes of the impacts are dominated by their gravity. The mass of the largest fragment (M_l) normalized

by the original mass of the target (M_t), i. e.,

$$f_l = \frac{M_l}{M_t} \tag{1.1}$$

has been widely used to characterize the degree of fragmentation in collisional events (e.g., Fujiwara *et al.*, 1977; Hartmann, 1978; Ryan *et al.*, 1991; Giblin *et al.*, 2004). As the specific impact energy (kinetic energy per target mass) increases for a given target, f_l will decrease ranging from $f_l > 0.9$ for cratering to $f_l < 0.1$ for complete fracturing. Giblin *et al.* (2004) adopted detailed values for classification of the degree of fragmentation. If $f_l > 0.9$, the outcome indicates cratering. If $0.3 < f_l < 0.5$, target is barely shattered. If $0.1 < f_l < 0.3$, target is shattered and if $f_l < 0.1$, target is highly shattered. Greenberg *et al.* (1978) defined $f_l = 0.5$ as the threshold value of "catastrophic disruption". It is the outcome where the largest fragment contains half the original mass and the energy density per target volume is defined as the impact strength.

1.2.2 Catastrophic disruption threshold, Q*

The most common scaling method in the previous literature to characterize collisional outcomes is determined by the impact strength which is the kinetic energy of the projectile normalized by the target volume or the specific impact energy which is the kinetic energy of the projectile normalized by the target mass. The term impact strength (Q*) was created by Greenberg and Hartmann (1977) to describe the energy density or specific kinetic energy, at which a given target material undergoes a fragmentation such that the resultant largest fragment has half the mass of the original body.

Davis *et al.* (1979) defined a threshold specific energy Q_D^* (impact kinetic energy per target mass) in developing an asteroid collisional evolution model. Q_D^* is required to both shatter mechanical bonds and accelerate half the mass to escaping trajectories. The specific energy to shatter, Q_S^* is defined as the total kinetic energy per unit mass of the target (or the sum of target and projectile) needed to produce the largest fragment that contains half of the original target mass. The shattered pieces may reaccumulate or not, depending on their velocity relative to the escape velocity. Shattering requires a lower specific energy $Q_S^* < Q_D^*$ to create fragments smaller than half the target mass. For small rocks $Q_D^* \rightarrow Q_S^*$, whereas for large bodies $Q_S^*/ Q_D^* \rightarrow 0$. When $Q_S^* \ll Q_D^*$, the probability of a shattering impact becomes far greater than

the probability of a dispersal, in which case an asteroid might be expected to evolve into a pile of rubble, unless other effects (such as melting and compaction) were to dominate. Davis *et al.* (1979) expressed impact strength as the sum of the shattering strength plus the gravitational binding energy of the target, i. e.,

$$Q_D^* = Q_S^* + \frac{4}{5}\pi\rho G R^2 \tag{1.2}$$

where R is the radius of a spherical target and ρ is its density. Equation 1.2 is called energy scaling. Figure 1.1 shows the relation between Q_D^* and R (Asphaug *et al.*, 2002). It plots as a horizontal line ($Q_D^* \approx Q_S^*$ = constant) in strength regime. Transitioning at some size, it plots as line of slope of 2 ($Q_D^* \propto R^2$) in gravity regime.

1.2.3 The role of physical properties of impacting bodies

Impacts include many parameters for example impact velocity and static strength, density, sound velocity of a body and so on. It is clear that the degree of fragmentation increases at higher impact velocities. There are three kinds of static strength for a brittle material; compressive, tensile, and shear strength. Fragmentation occurs when the weakest stress of them reaches the maximum sustainable level. Tensile strength of a material is used as typical strength on for impact disruption. To evaluate the results of impact experiments, the relation between impact strength and static strength of a target is used (e.g., Machii and Nakamura, 2011).

Porosity of a material is defined as $1-\phi$, where ϕ is volume filling factor (the ratio of bulk density to component density). Young's modulus and bulk modulus related to sound velocity are also important parameters.

Static strength and dynamical strength for rocky bodies

Housen and Holsapple (1999) demonstrated the size effect in collisional fragmentation of rock. As rocky targets, granite with a diameter variation of a factor of 18 (size from 1.9 to 34.4 cm in diameter) and tensile strength of $\sim 10^7$ Pa was used. If a sample were not completely homogeneous, its strength was determined by the weakest point. Larger samples might have the potential to include much weaker parts

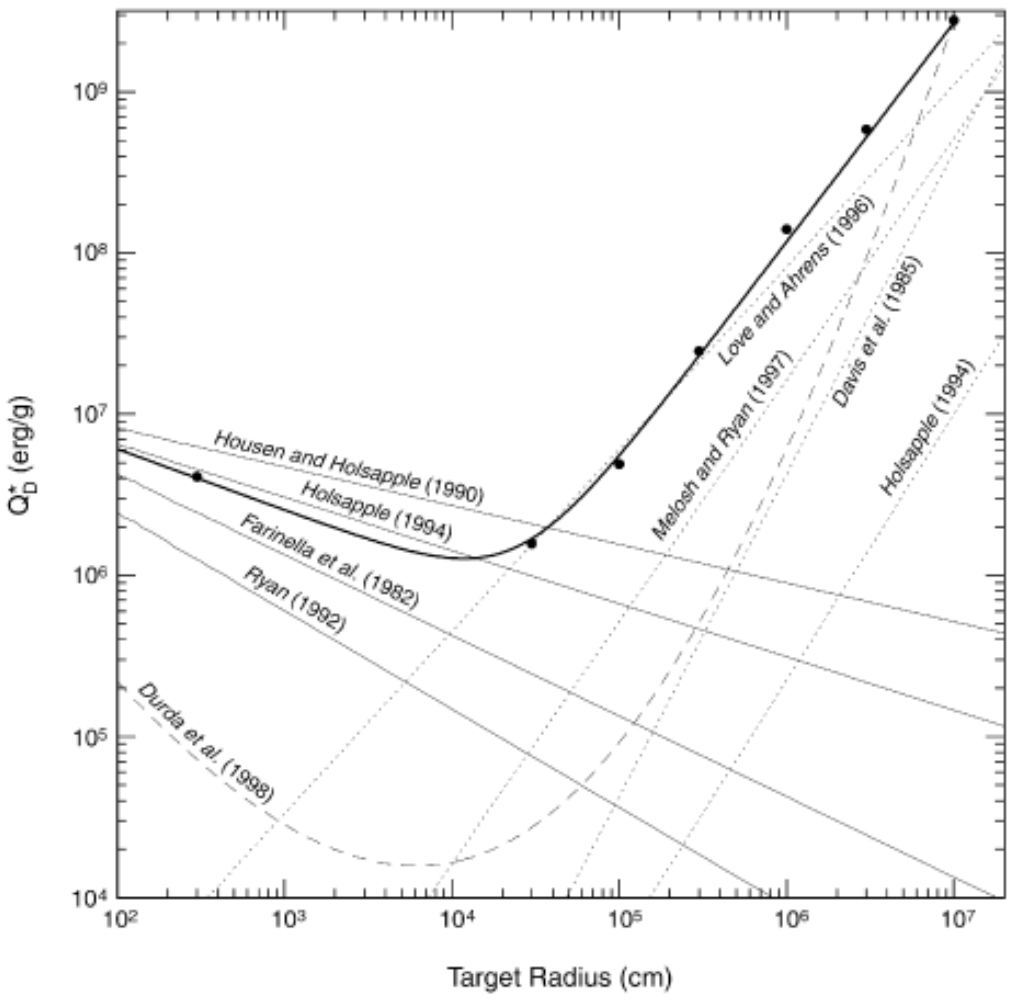

Figure 1.1: Cited from Asphaug *et al.* (2002). Values for the catastrophic dispersion threshold Q_D^* of asteroids vary widely in the literature. The region of slopes of 2 indicates gravity-dominant collisions. The region of negative slopes indicates strength-dominant collisions.

than the smaller samples, so that strength would decrease with increasing sample size. The concept that failure occurs due to growth and coalescence of internal flaws provided a number of theories of brittle fracture. From collisional outcomes the larger targets experienced much more collisional damage than the smaller targets. It was confirmed that impact strength decreases as size increases.

Various measurements of collisional outcomes and scaling models were provided by e.g., Gault *et al.* (1972), Fujiwara (1980), Housen and Holsapple (1990), Holsapple (1994) and Ryan and Melosh (1998). In model results shown in Figure 1.1, Q^* was more than two orders of magnitude of difference for asteroids 1 km in diameter.

Static strength and dynamical strength for porous bodies

There are a variety of internal structures for porous bodies. The types of internal structures were classified by previous works (e.g., Nakamura *et al.*, 2009). Aggregate-type structure consists of more than one components. If the aggregate consists of fine components, Wan der Waals' force between the components plays a role of bulk strength of the body. The type of coherent aggregate or coherent rubble-pile, certain glue, such as cement plays a role of cohesive force between the components. They are categorized differently from gravitational aggregate or gravitational rubble-pile in previous category (Richardson *et al.*, 2002). Or if components consist of ice, sintering also makes strong connections. For both types of bodies, component strength is stronger than bulk strength. Other types of structure are the pumice-like which include many voids in a body, and pre-shattered ones.

Specific energy density of porous bodies is larger than the rocky ones although they have the similar bulk strength (Love *et al.*, 1993; Nakamura *et al.*, 2009; Setoh *et al.*, 2010). This result is considered to be due to kinetic energy being spent to compress voids in the target and dissipated.

1.2.4 Common equations for impact experiments

Melosh (1989) summarized the basics for impact physics. The fundamental equations typically used for high velocity impact derived by P. H. Hugoniot in 1887. The equations are derived from the conservation of mass, momentum, and energy across the discontinuity. They are written as

$$\rho(U-u_p)=\rho U \tag{1.3}$$

$$P-P_0=\rho_0 u_p U \tag{1.4}$$

$$E-E_0=(P+P_0)(V_0-V)/2 \tag{1.5}$$

where P_0 and P are the pressures in front of and behind the shock front, u_p is the particle velocity, U is the shock velocity, ρ and ρ_0 are the compressed and uncompressed densities, E_0 and E are the specific internal energies, and V $(=1/\rho)$ and V_0 $(=1/\rho_0)$ are the compressed and uncompressed specific volumes, respectively.

In equation 4.3, there is linear relation between U and u_p and it is empirically represented by

$$U=C+Su_p \tag{1.6}$$

where C is the constant (usually close to the bulk sound speed) and S is the dimensionless parameter related to the Grüneisen parameter Γ at low pressure

$$S=(1+\Gamma)/2 \tag{1.7}$$

where Γ = α K_0 / ρ_0 C_v, in which α is the volume coefficient of expansion, K_0 is the zero pressure isentropic bulk modulus and C_v is the specific heat at constant volume.

In the case of impact experiments, normally P_0 = 0 and the equation 4.3 is represented as

$$P=\rho_0 u_p U. \tag{1.8}$$

Substituted U (the equation 1.6) into the equation 1.8,

$$P = \rho_0 u_p (C + S u_p). \tag{1.9}$$

If $u_p << C$, the equation 1.9 is represented as

$$P = \rho C u_p. \tag{1.10}$$

This thesis consists of studies on two themes, the impact disruption of sintered bodies and the formation process of the chondrite parent bodies. In chapter 2, I look at the effect of sintering for impact disruption. In chapter 3, impact experiments are performed with fluffy dust targets simulating a process formation process of chondrule parent bodies. I summarize the results from these studies in chapter 4.

Chapter 2

Experimental studies on the impact disruption of sintered bodies

2.1 Introduction

Many asteroids were found to have significant porosity. Some of them with large macroporosity may have a rubble pile structure (Britt *et al.*, 2002; Fujiwara *et al.*, 2006). Icy small bodies such as Kuiper Belt Objects (KBOs) and Saturn's small moons may also be rubble piles or aggregates (Trilling and Bernstein, 2006; Porco *et al.*, 2007). The response of impact for porous bodies is quite different from the response of dense rocky bodies due to the difference in the physical properties of materials as described in Chapter 1.

For an icy body having a rubble pile structure, if contact areas between constituents have physical connection due to sintering, they can have stronger bulk strength than those just bounded by van der Waals ' force and self-gravity. Sintering is a process that physically connects adjacent particles at temperature below the melting point. The process of sintering is contact between constituents, increase of the contact area, extinction of pores and finally grain growth. Driven force of sintering is surface energy. Surface tension of a solid material decreases its surface. Mass transfer by stress derived from surface tension occurs as sintering. There are mechanisms of mass transfer, viscous flow, evaporation-condensation and volume and surface diffusion. The connection point is called neck. In general, there is a power-law relation between the ratio of neck radius to particle radius and sintering duration or particle radius (e.g., Kingery and Berg, 1955; Poppe, 2003). The connected part between the particles is called neck. For the icy particles of radius 0.1 μm, it takes 0.15 year to have the neck radius of 0.08 μm at 100 K. This is a very short time scale compared to processes in a protoplanetary nebula, thus, it is possible for icy agglomerates to connect to each other by sintering (Sirono, 1999). The radiative equilibrium temperature in the region between the orbits of Jupiter and Saturn is about 100 K in the present. Hence, sintering is likely to proceed for icy aggregates or bodies consisting of fine particles in the vicinity of Jupiter and Saturn even at present.

The characteristics of agglomerated bodies are not only high porosity but also weaker bulk strength than the strength of the component materials. Such weaker bulk strength can be represented by RTS value less than 1, which is the ratio of the tensile strength of the object to the mean tensile strength of the components defined as relative tensile strength (Richardson *et al.*, 2002). In impact processes of small bodies, one of the significant parameters is the strength of the material, because the outcome of impact is strongly dependent upon the strength especially when the gravity is weak in comparison with the strength. A convenient measure characterizing collisional outcomes are the catastrophic disruption

thresholds (Q_S^* and Q_D^*) of the target. Laboratory impact experiments have shown that porous targets tend to have larger Q_S^* than coherent ones (Nakamura *et al.* 2009, and references therein). Setoh *et al.* (2010) conducted impact disruption experiments of sintered glass beads targets of about 40 % in porosity with different compressive strength (which means different RTS value) and showed that Q_S^* increases with the compressive strength of the target. However, the relationship between Q_S^* and the internal structure of these bodies, such as the size distribution of the components or the scale of the in-homogeneity, is still not clear. For example, when the scale of the in-homogeneity of the internal structure is not negligibly smaller than the size of the impacting bodies, the outcome of impact could be different from uniform, continuum medium (Cintala *et al.*, 1999). Another measure of the in-homogeneity of the internal structure would be the ratio of the typical component size to the target size. i.e., Relative Component Size to target size (RCS) defined as the ratio of the typical constituent radius to the target radius. Short period comets and ring particles are likely collisional fragments (Farinella and Davis, 1996; Charnoz *et al.*, 2009). If we consider collisional fragments from homogeneous sintered agglomerates of icy particles, the RCS value differs, according to the size of the fragments, although the porosity and the bulk tensile strength of the fragments are probably similar to the parent agglomerates and thus similar among the fragments. The RCS value of the previous impact experiments of porous sintered glass beads targets is of the order of $\sim 10^{-3}$ and much less than unity. The diameter of the constituent glass bead was 50 μm whereas the target diameter was a few to several centimeters (Love *et al.*, 1993; Michikami *et al.*, 2007; Setoh *et al.*, 2010).

Impact strength of porous ice targets with different internal structures at low impact velocities were previously investigated in comparison with solid ice targets and were found to be dependent upon the projectile material (Ryan *et al.*, 1999). Here we focus on the effect of static strength between components and the relative size of the components of sintered agglomerate targets on the impact disruption process. We first investigated the relation between neck growth and strength due to sintering. In Section 2.2 we describe our procedure on the strength measurement of sintered two equal-size particles (dimers). Section 2.3 describes the results of the measurement and observation of the dimers and agglomerates.

Then we conducted impact disruption experiments of sintered glass bead agglomerates with a fixed porosity, two different RTSs, and much larger RCS than previous studies. The result is discussed in comparison with the previous results of sintered glass beads of similar porosity but with much smaller RCS values (Setoh *et al.*, 2010), sintered pure ice targets (Arakawa *et al.*, 2002), and sintered ice-silicate

mixture targets (Arakawa and Tomizuka, 2004).

2.2 Experiments

2.2.1 Samples

In our experiments, glass beads were used. Sintering occurs under melting or softening temperature and is highly dependent on the temperature, therefore, controlling the sintering process, observing the neck radius, and conducting strength measurements for ice is difficult. On the contrary, soda-lime glass has its softening point at about 750 degree in centigrade, and is not affected by sintering at room temperature even for fine particles and is easy to be handled. Soda-lime glass is brittle at room temperature so as ice is under low temperature (Durham *et al.*, 2005), therefore it is expected that the physical characteristics of ice agglomerates, such as the relation between neck radius and static strength or the relation between static strength and impact strength can be qualitatively investigated using soda-lime glass.

We prepared two different samples; sintered dimers and agglomerates. Sintered dimers were used to measure the necessary force to break the neck between the particles. Two types of glass beads with different degree of surface roughness were used to investigate the effect of surface roughness on static strength. The one has a relatively rough surface and is 4.9 $\pm$ 0.1 mm in diameter and 0.161 $\pm$ 0.001 g in mass, and the other has a relatively smooth surface and is 4.70 $\pm$ 0.02 mm in diameter and 0.145 $\pm$ 0.003 g in mass. Figure 2.1 shows the one dimensional surface roughness of the particles measured using a laser displacement meter. Two beads of the same type were put into an alumina cylinder of 5 -0+0.2 mm in diameter and 20 mm long. The beads were heated for various durations at three different peak temperatures in an oven under atmospheric pressure. The sintering condition for dimers is summarized in Table 2.1. All were heated from room temperature to the peak temperature in one hour, whereas they were cooled in the closed oven after the heater was switched off which takes roughly a day. They were heated with and without an alumina sphere of about 4 mm in diameter put on the top of the glass beads as a weight in order to see if the additional weight accelerates the sintering process and strengthens the neck connection.

Two types of sintered agglomerate were prepared to see the effect of RCS which adopted the equivalent sphere radius for the disc shaped target on impact disruption. One has RCS of 0.19 and was made of the same smooth particles as the dimers because we found no difference in the bending strength between

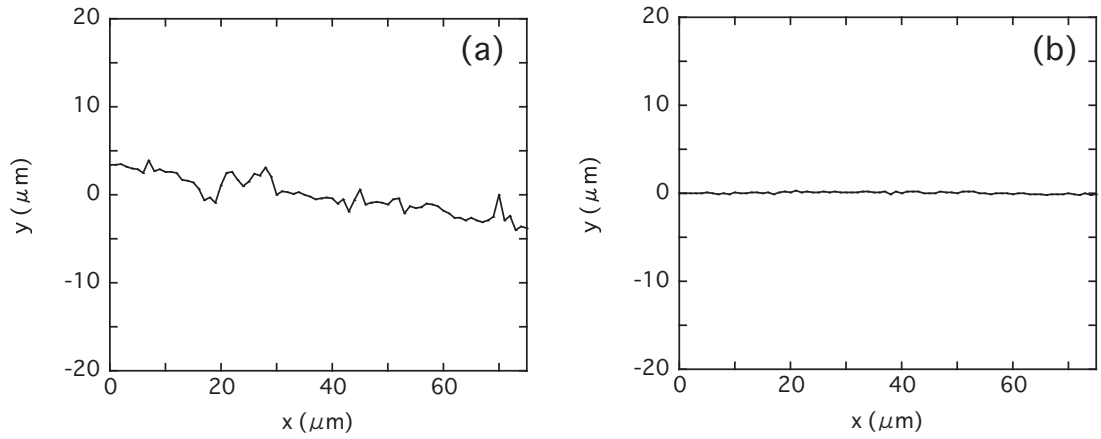

Figure 2.1: Surface roughness (y) of beads scanned by a laser displacement meter in one direction (x) with 1 μ m step for (a) a rough particle and (b) a smooth particle.

Table 2.1: The conditions of sintering for dimers

Particle type	Particle radius (mm)	Sintering condition	
		Peak temp. (°C)	Duration (h)
rough	4.9 ± 0.1	570	12, 20, 30, 45, 50, 60, 90, 120, 240
		600	4, 5.5, 8[*1], 12, 15, 20, 30, 40, 50, 60, 120
		630	0.5, 1, 2[*1], 4, 8[*1]
smooth	4.70 ± 0.02	630	0.5, 0.75, 1, 2, 4, 8, 20

[*1] Sintering with and without an alumina weight on the top of a dimer.

the smooth and rough particles with necks larger than ∼ 0.4 mm shown later in Fig. 2.5b. Beads were put into alumina hollow cylinders of about 30ϕ × 20 mm and 40ϕ × 30 mm. The beads in the alumina mold were heated using the oven at 600 or 630 °C under atmospheric pressure. Table 2.2 describes the sintering condition for agglomerates with RCS of 0.19. The temperature rise-time was one hour. Cooling was natural and its duration was about a day. The agglomerates consist of 90 particles. They have a three-layered-structure and each layer consists of 30 particles. The porosity of the agglomerates defined as the void space in a bounding cylinder was 39 ± 1% after sintering. We observed necks between the particles using a polarization microscope. Figure 2.2a shows an example of a sintered agglomerate.

The other has RCS of 0.027 which is the one order smaller than the previous agglomerates and consists of glass beads of 0.73 mm in average diameter. Beads were put into an alumina cylinder of about ϕ 30 × 20 mm. Table 2.3 describes the sintering condition for agglomerates with RCS of 0.027. The sample was

Table 2.2: Properties of agglomerates with RCS of 0.19

Sample name	Peak temp. (°C)	Duration (h)	Mass (g)	Porosity (%)	♯[*1]	Neck radius (mm)	Bulk tensile strength ($\times 10^5$ Pa)
ikura7	600	4	47	47	30	0.38 ± 0.11	0.388
ikura9	600	63	32.3	39	37	0.46 ± 0.13	2.46
100119	630	20	12.96	38	11	0.64 ± 0.13	-[*3]
100219	630	20	12.96	39	20	0.76 ± 0.13	-[*3]
100223	630	8	12.97	39	23	0.53 ± 0.11	-[*3]
100311	630	8	12.96	38	-	-[*2]	-[*3]
100329	630	8	12.96	39	-	-[*2]	-[*3]
100314	630	20	12.98	37	51	0.52 ± 0.20	-[*3]
100301	630	8	12.98	39	43	0.39 ± 0.14	-[*3]
100403	630	8	12.97	39	-	-[*2]	-[*3]
100412	630	8	12.97	40	-	-[*2]	-[*3]
100413	630	8	12.97	39	-	-[*2]	-[*3]
100414	630	8	12.97	38	-	-[*2]	-[*3]
100416	630	8	12.98	39	-	-[*2]	-[*3]
100331	630	8	12.96	39	-	-[*2]	2.72
100427	630	8	12.97	39	30	0.34 ± 0.12	4.73
100428	630	8	12.96	35	-	-[*2]	3.09
100507	630	20	12.95	37	92	0.47 ± 0.12	8.75
100511	630	8	12.96	40	87	0.32 ± 0.09	3.5
100512	630	8	12.97	39	78	0.30 ± 0.10	3.16
100513	630	20	12.96	33	88	0.48 ± 0.14	5.77
100515	630	20	12.93	34	-	-[*2]	7.7
100627	630	8	12.96	40	-	-[*2]	-[*3]
100706	630	8	12.95	36	-	-[*2]	-[*3]
100712	630	8	12.97	37	-	-[*2]	-[*3]
100704[*4]	630	8	12.82	37[*5]	-	-[*2]	-[*3]
100710[*4]	630	8	12.82	37[*5]	-	-[*2]	-[*3]
100812	630	20	13.00	36[*5]	-	-[*2]	-[*3]
100814	630	20	13.01	37[*5]	-	-[*2]	-[*3]
20110531	630	20	13.00	36	-	-[*2]	-[*3]
20110603	630	20	12.98	37	-	-	-
20110607	630	20	12.55	35	-	-[*2]	-[*3]
20110609	630	20	12.85	37	-	-[*2]	-[*3]
20110613	630	20	12.80	36	-	-[*2]	-[*3]
20110615	630	20	12.49	35	-	-[*2]	-[*3]
20110622	630	20	12.8	35	-	-[*2]	-[*3]
20110629	630	20	12.96	37	-	-[*2]	-[*3]
20110704	630	20	12.83	36	-	-[*2]	-[*3]
20110708	630	20	12.96	34	-	-[*2]	-[*3]
20110711	630	20	12.94	36	-	-[*2]	-[*3]

[*1] Number of necks for which radius was determined.
[*2] Neck radius has not been measured.
[*3] Agglomerates used for impact disruption experiments.
[*4] Agglomerate with 89 particles. One of original 90 particles was separated when the agglomerate was taken from the mold.
[*5] The porosity expected for the agglomerate with original 90 particles.

Table 2.3: Properties of agglomerates with RCS of 0.027

Sample name	Peak temp. (°C)	Duration (h)	Mass (g)	Porosity (%)
20110720	650	20	73.60	38
20110828	650	8	74.57	37
20110902small1	650	4	75.75	39
20110902small2	650	4	76.00	39
20110929small	650	4	15.69	40
20110930small	650	4	17.55	41
20111001small1	650	4	17.59	41
20111001small2	650	4	16.90	41
20111003small	650	4	17.78	40
20111004small	650	4	16.71	40
20111005small1	650	4	17.58	40
20111005small2	650	4	17.45	41
20111006small1	650	4	18.49	40
20111006small2	650	4	18.64	41
20111007small1	650	4	19.67	41
20111007small2	650	4	18.13	41
20111008small	650	4	17.20	40
20111009small1	650	4	18.95	40
20111009small2	650	4	20.53	40
20111010small1	650	4	18.84	41
20111010small2	650	4	21.13	43
20111011small	650	4	17.45	42
20111012small	650	4	18.52	40

heated using the oven at 650 °C under atmospheric pressure. The porosity of the agglomerates was 40 % after sintering.

2.2.2 Static measurements of dimers

Images of the sintered dimers were taken by the microscope with the following procedure. The dimer was put on the stage of the microscope and observed in a direction horizontal to the neck cross section. The strength of dimers was measured against tensile (normal) force or bending (tangential) force. The tensile force measurements were performed for the dimers consisting of the rough surface particles using a uniaxial compression testing machine. Strings were glued to the top and the bottom of the dimer with instant adhesive as shown in Fig. 2.2b and were pulled at a rate of 0.001 mm/s. For the dimer with larger neck radius and stronger tensile strength, the measurement was conducted using a jig described in Fig.

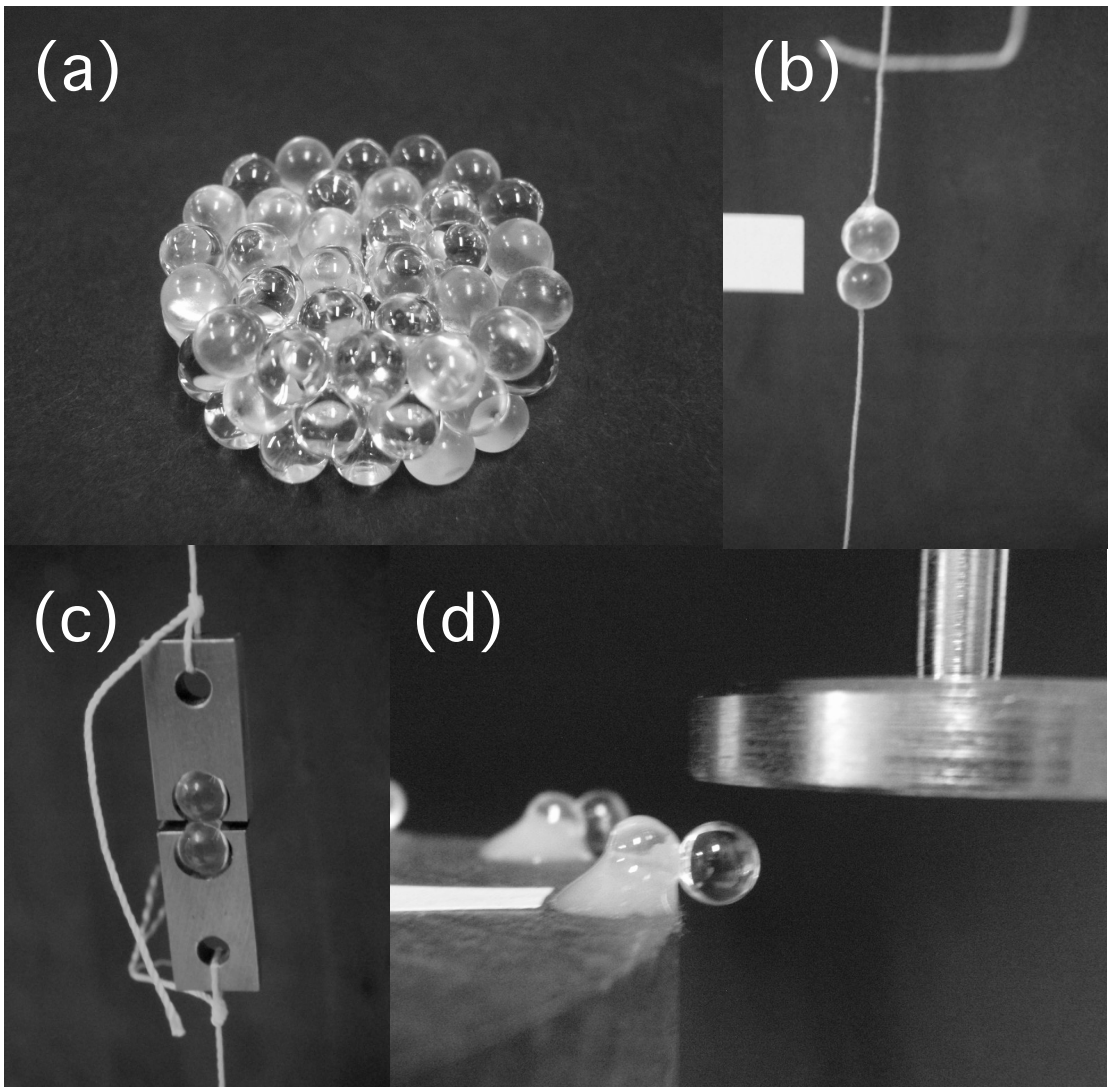

Figure 2.2: Images of sintered glass beads. (a) An example of agglomerates, (b) tensile test of a dimer with glued strings, (c) tensile test of strong dimer with a jig, and (d) bending test of a dimer.

2.2c.

The bending force measurements were conducted for both dimers consisting of the smooth particles and the rough particles. Figure 2.2d shows the configuration of the measurement. One of particles was fixed with adhesive on an iron cylinder of about 6 kg. The other was forced downward using the testing machine.

2.2.3 Static strength measurements of agglomerates

The properties of the agglomerates of RCS = 0.19 are shown in Table 2.2. Bulk tensile strength of the agglomerates of RCS = 0.19 was measured by Brazilian disc test in which external compressive force was applied to the agglomerates from their side using the strength testing machine at the loading rate of 0.001 mm/s. They were broken into two major pieces by internal tension induced by compression. The tensile strength of the agglomerates is given as;

$$\sigma_t = \frac{2F}{\pi dl}, \tag{2.1}$$

where F denotes the maximum applied force, d and l denote the diameter and the thickness of the agglomerate, 37.29 mm and 28.71 mm for ikura7, 38.65 mm and 17.9 mm for ikura9 and about 30 mm and about 12 mm for the rest, respectively. Neck radii of agglomerates were measured before or after conducting the Brazilian disc test using the microscope.

For the agglomerates of RCS = 0.027, there was a difficulty to conduct Brazilian disc test. Because of roughness on testing surface, applied force was concentrated on the most salient particle. They were not broken into two major pieces and the test was failed. Therefore a piece of sponge with thickness of 5 mm was fixed at the top and the bottom of the agglomerate and then the agglomerate were broken into two major pieces.

2.2.4 Dynamic strength measurements of agglomerates

Impact experiments were performed by a helium gas-gun installed at Kobe University with projectile velocities similar to most of the previous disruption experiments on sintered glass bead targets of similar porosity, but different RCS (Setoh *et al.*, 2010). For head-on collision experiments, two types of sintered agglomerates, RCS of 0.19 and 0.027 were used as targets. Projectiles were cylindrical polycarbonate of 3 mm in diameter, 6 mm in length and a soda-lime glass sphere of about 3 mm in diameter. Oblique (45° declined to a trajectory) and edge-on (side surface of cylindrical target) impact experiments were also performed to examine a possible shape effect. In these cases, stronger agglomerates with RCS of 0.19

were used as targets. Two high-speed cameras were used. One (Shimazu HPV-2) took images at 8-64 μs per frame to observe a projectile impacting the target, while the other (Photron FASTCAM SA1.1) was 100-185 μs per frame to observe the disruption of the target.

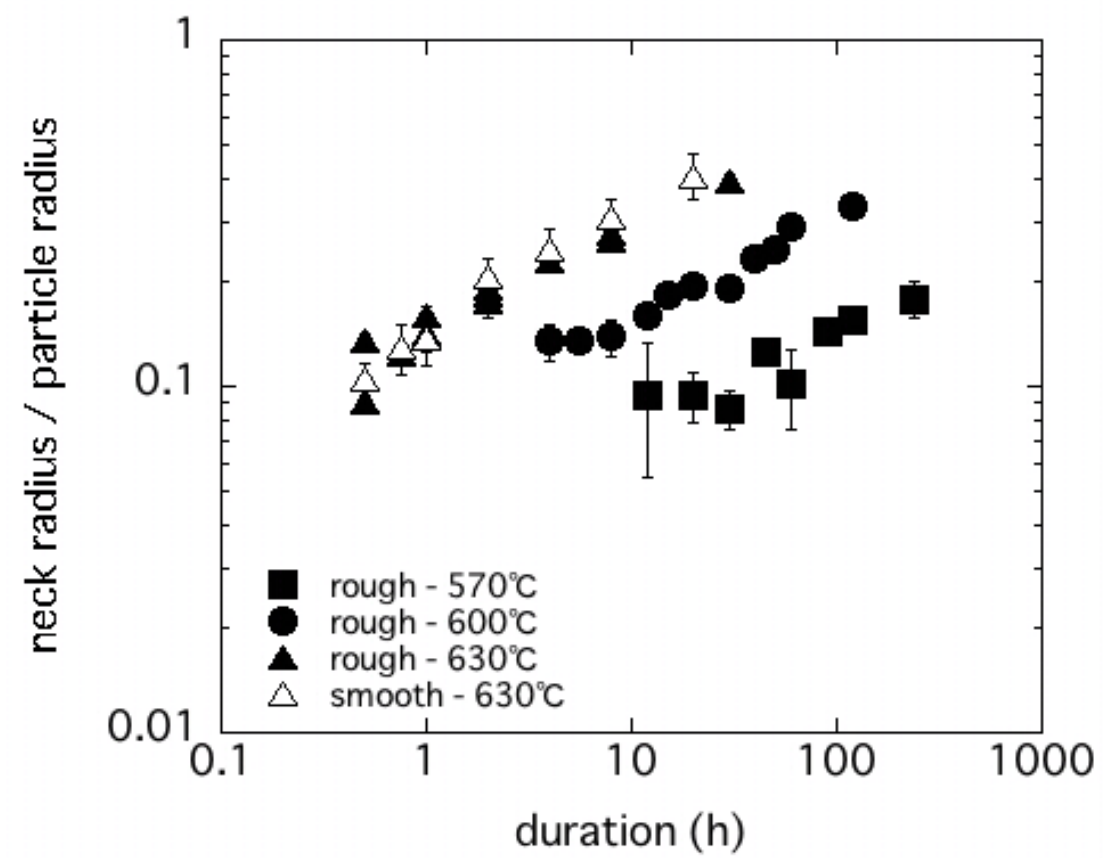

Figure 2.3: Normalized neck radius versus sintering duration with peak temperature of 570 °C (filled square), 600 °C (filled circle), and 630 °C for the smooth (open triangle) and the rough particles (filled triangle).

2.3 Results

2.3.1 Physical properties of sintered samples

Figure 2.3 shows the relation between normalized neck radius and heating duration for sintered dimers. The neck grows larger at higher peak temperature and longer heating duration.

Generally, neck growth is represented by a power law of heating duration. Even while temperature is increasing to the peak value and decreasing to the room value, the necks should grow. We assume following equation for the neck growth,

$$\frac{x}{r} = at^b + c \tag{2.2}$$

where, x is neck radius, r is particle radius, t is the duration at the peak temperature and c is a component corresponding to the neck growth before and after peak temperature. We especially estimate the neck growth during rise time and cooling time for the sintering at 630 °C, because the rise time from the room temperature to the peak was half of the minimum duration at the peak temperature and the cooling time was even longer. We obtained $c = 0.085 \pm 0.083$ for the rough particles. Thus we neglect the neck growth before and after the peak temperature for all cases.

The power-law indices, b for the rough particles is 0.33 ± 0.01, 0.30 ± 0.02, and 0.30 ± 0.05 when heated at 630 °C, 600 °C, and 570 °C, respectively. The power-law index for the smooth particles is 0.37 ± 0.04 when heated at 630 °C. The power-law indices indicate that the sintering is driven by volume diffusion or evaporation-condensation under these conditions (Kingery and Berg, 1955).

Figure 2.4a compares the results of the dimers produced with and without the alumina weight. The neck radius of the dimers with the weight grows larger and have smaller dispersion in tensile force to break. As the necks grow larger, the critical tensile force to break becomes to have smaller dispersion for both types of the dimers, indicating that the grain boundary may be more perfectly connected and have more homogeneous structure.

Figure 2.4b shows the similar relation for all the dimers made with the weight. In general, the strength of the connection should increase in proportion to its cross section i.e., square of the neck radius. In the present result of the rough particles, regardless of the heating temperature, the critical tensile force to break is proportional to the square of the neck radius only if it is larger than ~ 0.4 mm.

Figure 2.5a indicates the examples of the relation between bending force and displacement for the weaker and stronger dimers. The energy needed to break the neck in the bending test is calculated by the area of the triangle: The average values are $E_{bend} = (1.6 \pm 1.9) \times 10^{-4}$ and $(5.6 \pm 4.4) \times 10^{-4}$ J for the weaker and the stronger agglomerates, respectively. According to Figure 2.5b, the critical bending force needed to break the neck is an order of magnitude smaller than the critical tensile force when neck is small, but approaches to the critical tensile force as the necks grow. The critical bending force is proportional

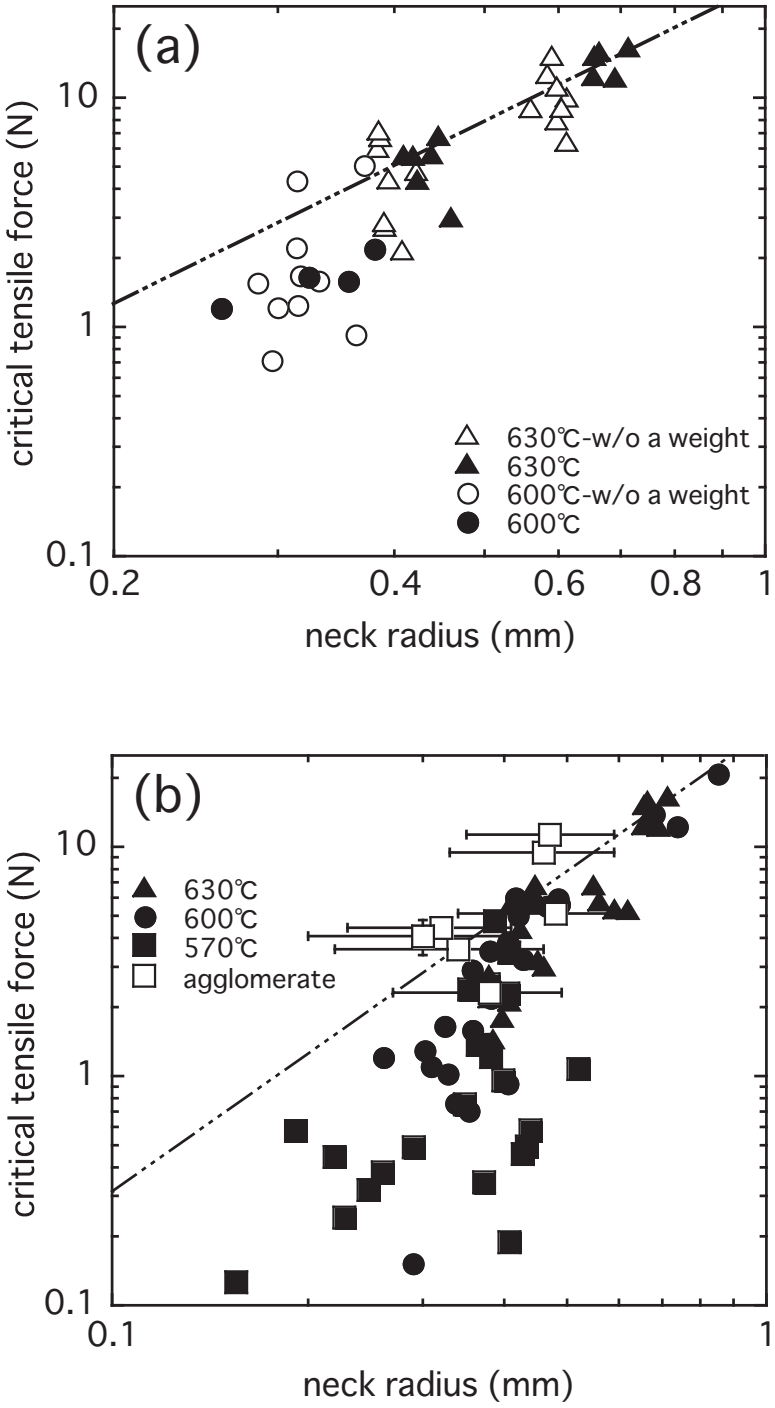

Figure 2.4: (a) Difference in neck radius and strength for sintering with (filled triangles and circles) and without (open triangles and circles) an alumina weight on the top of a glass particle. (b) Relation between neck radius and critical tensile force to break the neck of a dimer (filled marks) and an agglomerate (open square). Dashed line is a reference showing square dependence of the force on the neck radius.

to 3.0 ± 0.2 power of the neck radius for the smooth particles. For those with neck radius larger than $\sim$ 0.4 mm, there is no difference between the smooth and the rough particles. On the other hand, for those with neck radius smaller than $\sim$ 0.4 mm, the rough particles need much smaller forces to break than the smooth ones.

As shown in Figure 2.4b and 2.5b, both of critical tensile and bending forces for the rough particles are scattered when neck radius is smaller than $\sim$ 0.4 mm. The cross sections of the necks of the rough particles are shown in Figure 2.6. The cross section of the necks grown by shorter heating duration indicates imperfect connection. Moreover, some pores are appeared on the neck cross section. On the contrary, the cross section of the necks grown by longer heating duration has rather homogeneous structure with only little pores. The inhomogeneous structure of the necks of the rough particles shown by the microscope images is in consistent with the more scattered tensile and smaller bending strength of the rough particles with necks of radius less than $\sim$ 0.4 mm.

The tensile stress needed to break ikura7 and ikura9 is derived using equation 2.1, while average neck radius was obtained by observation of the necks or broken cross-sections. After conducting Brazilian disc test, number of broken necks were counted for each agglomerate. The average tensile force per neck at the break of the agglomerate is obtained as the value of the bulk tensile strength multiplied by the cross section of the agglomerate ($d \times l$) and divided by the number of broken necks. The average tensile force per neck for each agglomerate is shown in Figure 2.4b, indicating that the force necessary to break an agglomerate into two is approximately the sum of the tensile force necessary to break each neck in the cross section of the disc. The agglomerates from 100331 to 100515 were also applied Brazilian disc test although the thickness to diameter ratio is smaller for a standard measurement. The bulk tensile strength of the agglomerates of 8 and 20 hour-sintering is $3.53 \pm 0.87 \times 10^5$ and $7.4 \pm 1.5 \times 10^5$ Pa, respectively. These data are also converted and plotted in Figure 2.4b showing that the necks in the agglomerates have similar tensile strength to those of dimers and two other agglomerates (ikura7 and ikura9).

The tensile strength of sintered agglomerates with RCS of 0.027 is $2.9 \pm 1.54 \times 10^5$ Pa from the measurement with sponge as shown in Table 2.4. Additionally, the tensile strength of agglomerates with RCS of 0.19 for 8 and 20 hour-sintering were also measured with sponge as shown in Table 2.4 and was $4.1 \pm 1.9 \times 10^5$ and $3.7 \pm 0.6 \times 10^5$ Pa, respectively. From the results of RCS of 0.19, the difference

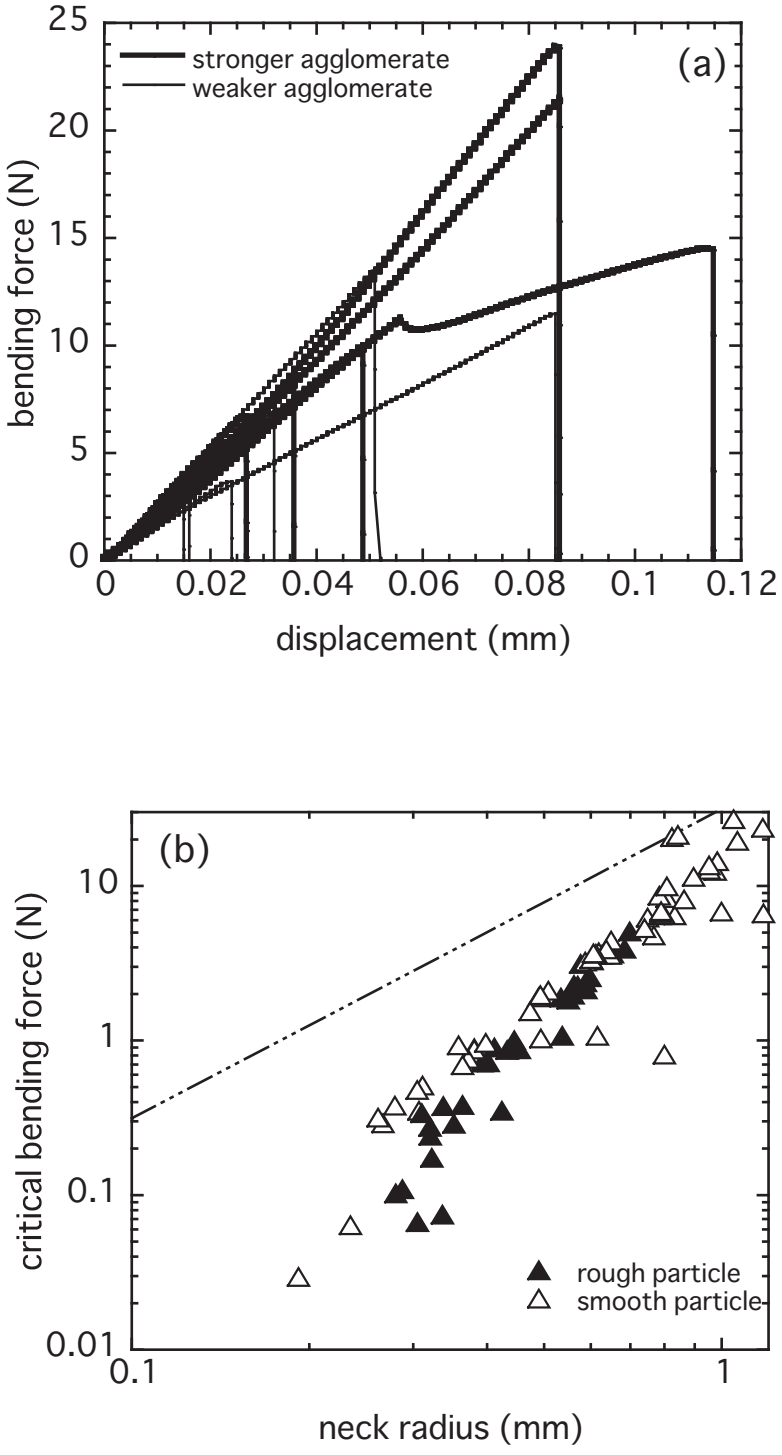

Figure 2.5: (a) Examples of the relation between displacement and bending force for dimers. (b) Relation between neck radius and critical bending force to break the neck of a dimer of the rough particles (filled triangles) and the smooth particles (open triangles). Dashed line is a reference showing square dependence of the force on the neck radius.

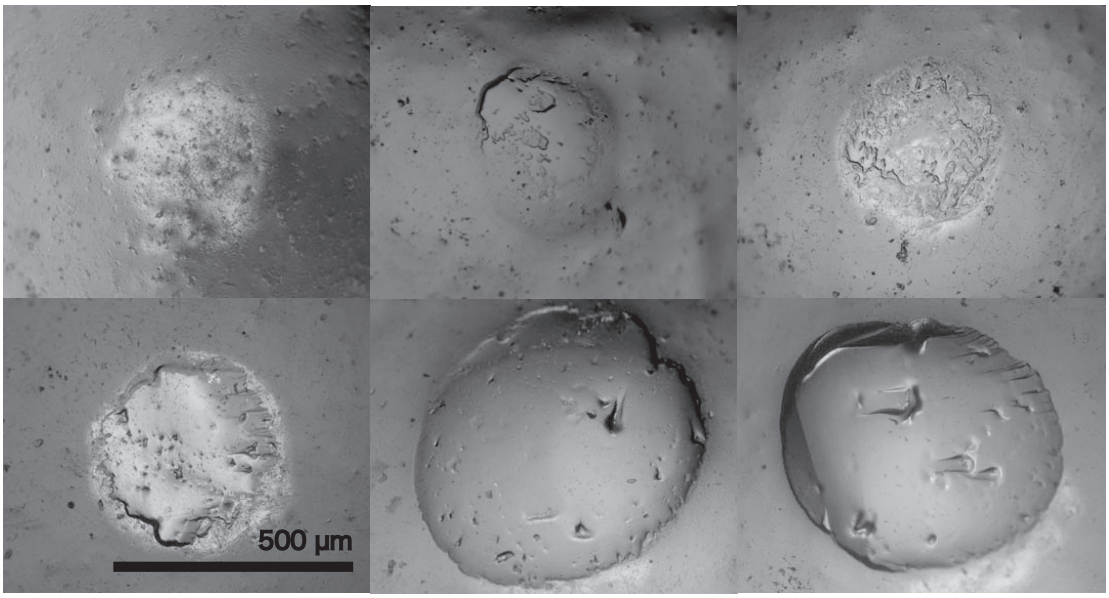

Figure 2.6: Texture of the neck cross section. Top, from left to right: 12 hours at 570 °C, 8 hours at 600 °C, 0.5 hour at 630 °C. Bottom, from left to right: 240 hours at 570 °C, 60 hours at 600 °C, 4 hours at 630 °C. Scale-bar = 500 μm.

between the measurement results with and without sponge was within the range of error bar.

2.3.2 Results of impact experiments

We performed head-on impact experiments on sintered agglomerates which had two different tensile strengths and RCS value of 0.19 and 0.027, where the equivalent sphere radius is adopted for the disc shaped target. Targets were mostly broken at the necks. For the agglomerates with RCS of 0.19, only a few or several particles were broken into fragments. Figure 2.7 shows the high-speed camera images of two different shots. The results of the experiments are summarized in Table 2.5. Type A target is the stronger one, type B is the weaker one and type C is the smaller component one (RCS = 0.027). For type A and B targets, off-centered impacts within 5 mm from the center of the targets are denoted by italic letter, while those beyond 5 mm are denoted by the letter with underline. Q_S^* is obtained using the data of the central shots and smaller off-center shots by fitting a power law to the relationship between the largest fragment mass fraction and collisional specific energy shown in Figure 2.8. Note that we do not include the data where the target was intact.

Table 2.4: Tensile strength measurements with sponge

Sample name	Peak temp. (°C)	Duration (h)	average diameter (m)	average hight (m)	Porosity (%)	Bulk tensile strength ($\times 10^5$ Pa)
20110720	650	20	0.030	0.012	39	2.76
20110902small5	650	6	0.039	0.015	-[a]	2.55
20110904small4	650	4	0.030	0.014	-[a]	1.62
20100715	630	8	0.030	0.012	39	2.62
20100723	630	8	0.030	0.012	38	1.89
20110902small3	650	6	0.050	0.022	38	4.14
20110704	630	20	0.030	0.012	36	3.25
20110708	630	20	0.030	0.012	34	4.11
20091023	630	8	0.039	0.016	-[a]	3.12
20110904small5	650	6	0.039	0.017	-[a]	1.67
20110904small3	650	4	0.050	0.022	39	2.92[b]
20110713small	650	4	0.050	0.025	-[a]	1.18
20110904small2	650	4	0.050	0.028	39	4.43
20110913	630	8	0.030	0.012	36	5.68
20110914	630	8	0.030	0.012	38	3.82
20110915	630	8	0.029	0.012	35	4.02
20110916	630	8	0.030	0.012	36	7.46
20110929small	650	4	0.030	0.015	40	3.41[b]

[a] No mass data
[b] Measurement failed.

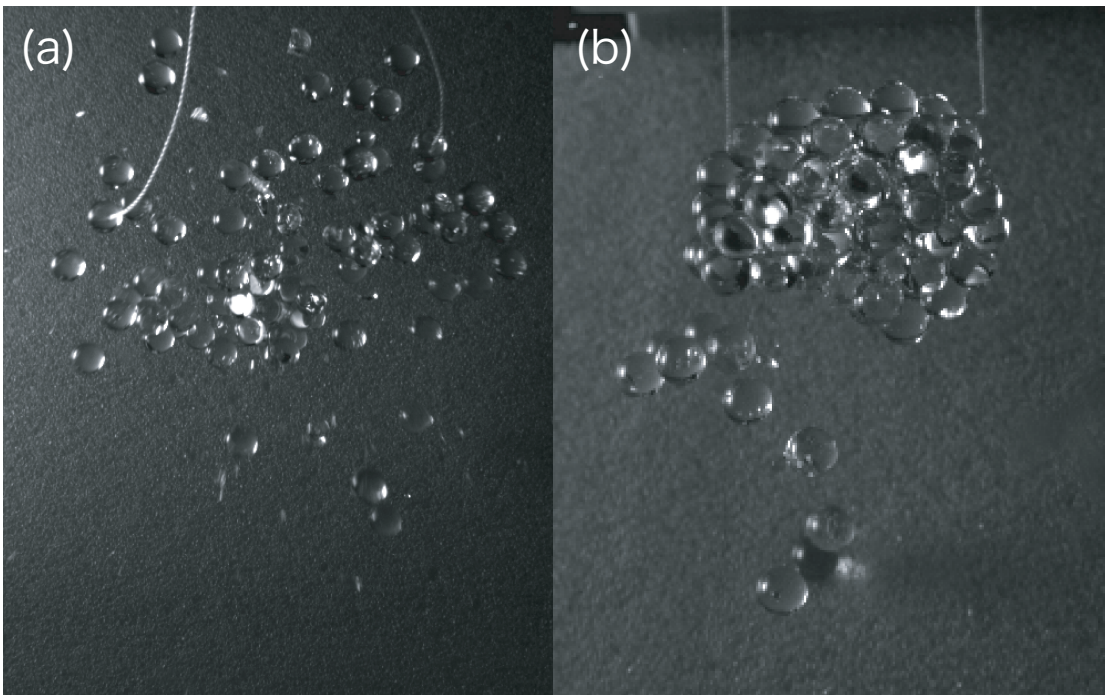

Figure 2.7: Images of impact disruption taken by a high-speed camera which fixed about 25 degree downward from ballistic plane. (a) An example for catastrophic disruption (target: 100412, M_l/M_t = 0.200, v_{imp}=150 m/s, 21.5 ms after the impact). (b) An example for moderate fragmentation (target: 100710, M_l/M_t = 0.853, v_{imp}=62 m/s, 35.7 ms after the impact).

Table 2.5: Summary of impact experiments

Sample name	Target type	Projectile type	Projectile mass (g)	Projectile size (mm)	Impact velocity, v_{imp} (m/s)	M_l/M_t[*3]
100119	A[*1]	sphere	0.0429	3.16	277	0.100
100219	A[*1]	cylinder	0.051	3.01 × 5.98	*153.7*[*2]	0.157
100314	A[*1]	sphere	0.0382	3.07	78	0.517
100223	B[*1]	cylinder	0.0515	3.01 × 6.04	*227.87*[*2]	0.0547
100311	B[*1]	sphere	0.0355	3.01	91	0.344
100329	B[*1]	sphere	0.0386	3.11	69[*2]	0.145
100301	B[*1]	sphere	0.0378	2.97	*60*[*2]	0.289
100403	B[*1]	sphere	0.0375	3.05	81[*2]	0.522
100412	B[*1]	sphere	0.0349	2.98	*150*[*2]	0.200
100413	B[*1]	sphere	0.0369	3.02	184[*2]	0.544
100414	B[*1]	sphere	0.0372	3.02	164	0.122
100416	B[*1]	sphere	0.0338	2.95	172	0.378
100627	B[*1]	sphere	0.0306	2.84	18[*2]	1.000
100706	B[*1]	sphere	0.0312	2.77	41[*2]	0.833
100712	B[*1]	sphere	0.0296	2.8	37	1.000
100704	B[*1]	sphere	0.0328	2.91	66	0.303
100710	B[*1]	sphere	0.0325	2.89	62	0.853
100712	A[*1]	sphere	0.0355	2.85	60	0.889
100714	A[*1]	sphere	0.0378	2.90	152	0.322
20110828small	C[*1]	sphere	0.0433	3.15	287	0.991
20110902small1	C[*1]	sphere	0.0433	3.15	244	0.980
20110902small2	C[*1]	sphere	0.0433	3.15	249	0.990
20110904small1	C[*1]	sphere	0.0433	3.15	266	0.978
20110930small	C[*1]	sphere	0.0433	3.15	278	0.424
20111001small1	C[*1]	sphere	0.0433	3.15	261	0.195
20111001small2	C[*1]	sphere	0.0335	2.92	50	0.989
20111003small	C[*1]	sphere	0.0304	2.85	37	0.992
20111004small	C[*1]	sphere	0.0433	3.15	178	0.477
20111005small	C[*1]	sphere	0.0430	3.15	183	0.840
20111005small2	C[*1]	sphere	0.0430	3.15	*156*[*2]	0.955
20111006small1	C[*1]	sphere	0.0430	3.15	*157*[*2]	0.839
20111006small2	C[*1]	sphere	0.0430	3.15	*159*[*2]	0.884
20111007small1	C[*1]	sphere	0.0430	3.15	238	0.107
20111007small2	C[*1]	sphere	0.0430	3.15	*183*[*2]	0.215
20111008small	C[*1]	sphere	0.0430	3.15	237	0.138
20111009small1	C[*1]	sphere	0.0430	3.15	190	0.452
20111009small2	C[*1]	sphere	0.0430	3.15	194[*2]	0.833
201110010small1	C[*1]	sphere	0.0430	3.15	*193*[*2]	0.925
201110010small2	C[*1]	sphere	0.0430	3.15	194	0.929
201110011small	C[*1]	sphere	0.0430	3.15	216	0.271
201110012small	C[*1]	sphere	0.0430	3.15	*216*[*2]	0.484

[*1] Type A: stronger target with RCS of 0.19. Type B: weaker target with RCS of 0.19. Type C: target with RCS of 0.027.

[*2] Italic letter denotes off-center impact within 5 mm from the center. Underlined letter denotes off-center impact beyond 5 mm from the center.

[*3] M_l: largest fragment mass, M_t: target mass

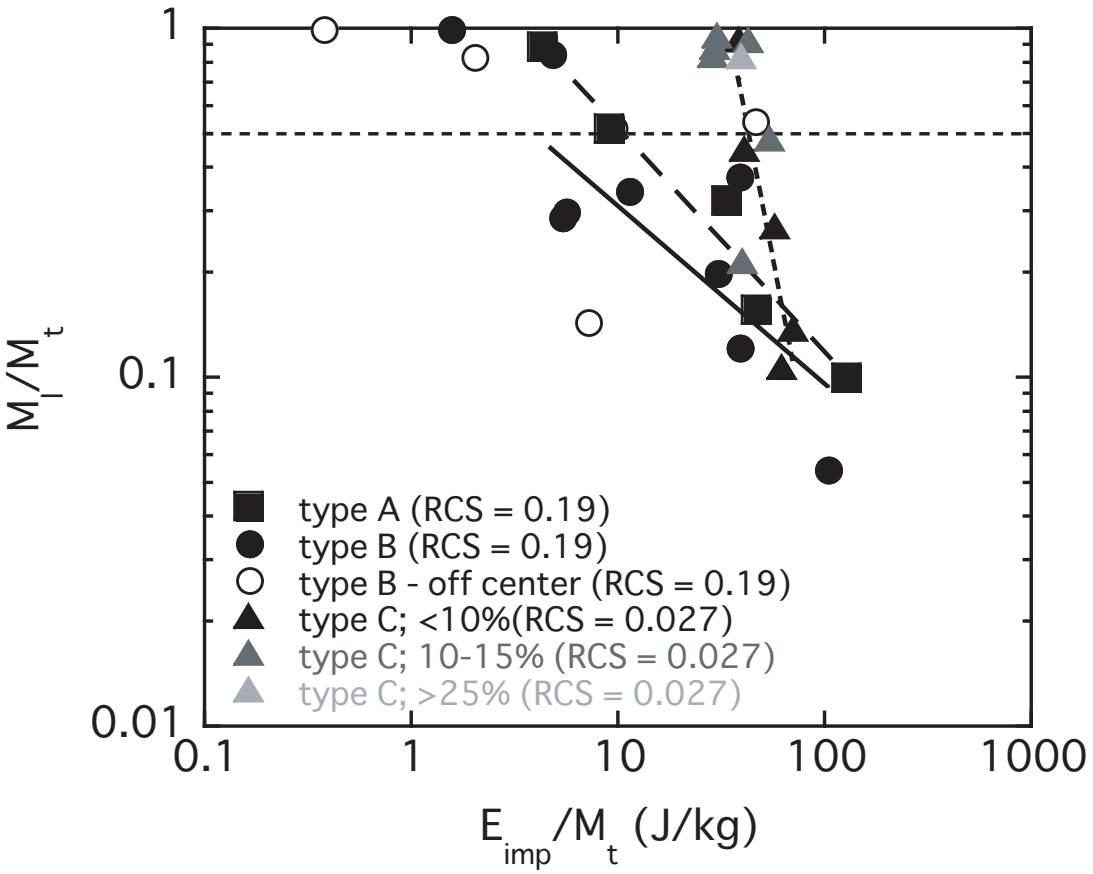

Figure 2.8: The relation between normalized largest fragment mass and specific collisional energy for head-on collision is represented. Filled squares indicate type A target data, filled circles indicate type B target, open circles indicate type B target with off-center collision and filled triangles indicate type C target. The degree of off-center collision was represented by color gradation. Denser color shows central collision.

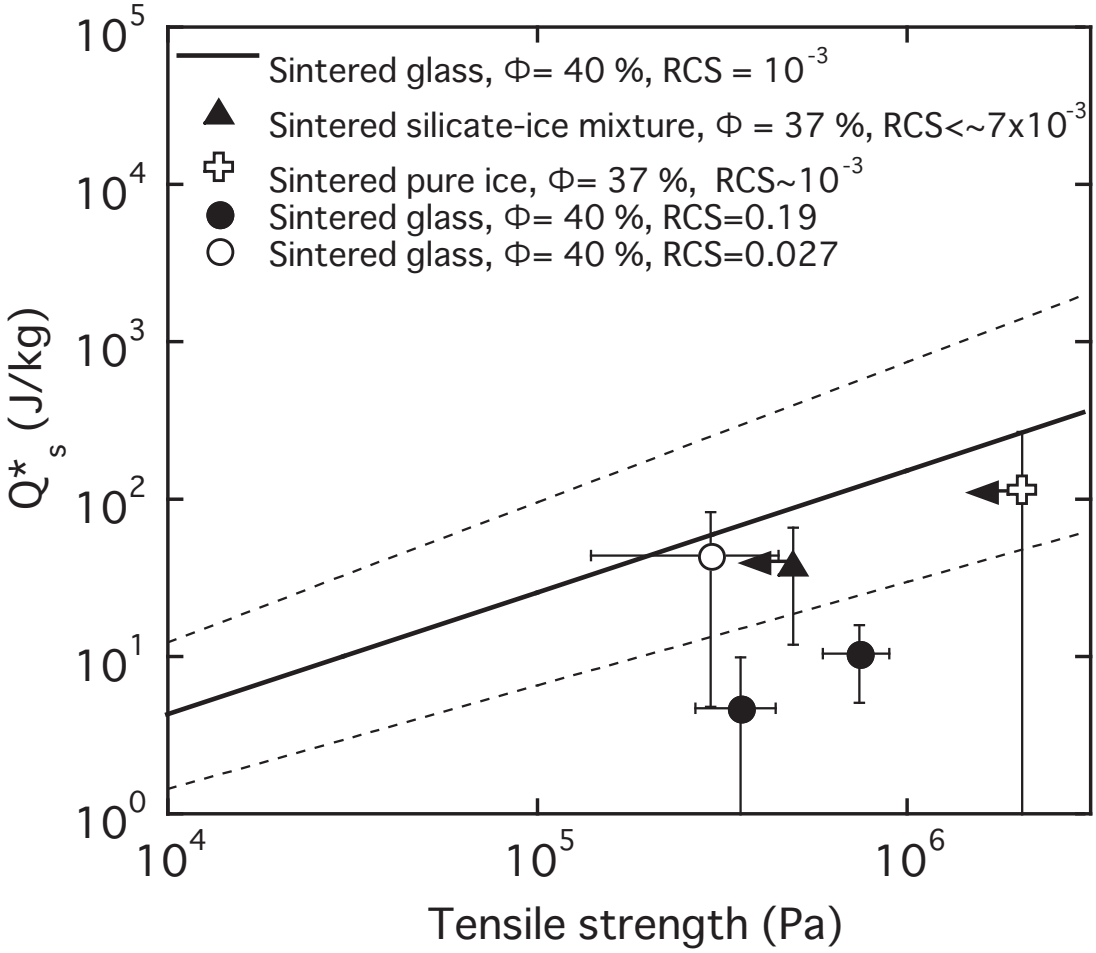

Figure 2.9: Impact strength versus tensile strength. Filled circle is the data of this work for the sintered glass target which have the porosity of 40 % and RCS of 0.19. Open circle is the data of this work for the sintered glass target which have the porosity of 40 % and RCS of 0.027. Previous results of different RCS values are also shown. Line is a fit to the data of low velocity impact disruption of porous sintered glass targets which have the porosity of 40 % and RCS of $\sim 10^{-3}$ (Setoh *et al.*, 2010). The large scatters the data have are indicated by the dashed line. Filled triangle is the data of sintered mixture ice targets which have the porosity of 37 % and RCS of $<\sim 7 \times 10^{-3}$ (Arakawa and Tomizuka, 2004). Open cross is the data of sintered pure ice targets which have the porosity of 37 % and RCS of $\sim 10^{-3}$ (Arakawa *et al.*, 2002).

Q_s^* for type A, type B and type C targets are 4.7 ± 5.8 and 10.6 ± 4.9 and 44.2 ± 39.4 J/kg, respectively. The results are shown in Figure 2.9 with previous results of Setoh *et al.* (2010) for the impact strength of sintered glass agglomerates which have porosity of ~ 40 % and RCS value of $\sim 10^{-3}$, those of Gault and Wedekind (1969) for single solid glass spheres, Arakawa *et al.* (2002) for sintered pure ice targets which have porosity of 37 % and RCS value of $\sim 10^{-3}$, and Arakawa and Tomizuka (2004) for sintered ice-silicate mixture targets which have porosity of 37 % and RCS value of $<\sim 7 \times 10^{-3}$. For the previous data of Setoh *et al.* (2010) and Gault and Wedekind (1969), we converted the compressive strength and ultimate strength given in the references to tensile strength by multiplying a factor of 0.17 according to the ratio obtained for porous sintered glass beads targets (Hiraoka, 2008). The ratio of compressive strength to tensile strength for pure ice and mixture ice targets with porosity of several % is 0.14 and 0.25, respectively (Hiraoka *et al.*, 2008). We adopt the compressive strength of 0.5 MPa and 2 MPa as the upper limit to the tensile strength for the porous ice-silicate mixture targets and the porous pure ice targets. Figure 2.9 shows that Q_S^* at a given tensile strength is identical for agglomerates of different materials, i.e., glass, pure ice, and ice-silicate mixture, but with RCS value less than 0.01. Q_S^* of the glass agglomerates of RCS = 0.19 is about one order of magnitude smaller than the previous results, while the glass agglomerates of RCS = 0.027 have almost the same Q_s^* as the previous results. This difference is probably due to number of component particles. If a target consists of small number of particles, stress wave meets less number of necks and therefore can transmit more energy through out the target. Also, the larger fraction of the surface particles enables the particles to move more freely and thus can be broken more easily.

The tendency seems similar to what was found for the growth efficiency for head-on collisions of Ballistic particle-cluster aggregation (BPCA) clusters of dust aggregates (Wada *et al.*, 2009), although the collision is for equal size aggregates, i.e., projectile size changes according to the target size, which is different from the present impact condition. They found that the larger is the number of constituent particles of BPCA cluster, the harder against disruption. The result implies that icy agglomerates of smaller number of constituent particles (i.e., those with larger RCS values), for example, smaller pieces of fragments from sintered agglomerates, may have smaller Q_S^* value than those with similar porosity and bulk tensile strength but much larger number of constituent particles.

Figure 2.10 shows the relation between normalized largest fragment mass and impact energy (E_{imp}) normalized by minimum bending energy to break all necks for an agglomerate. We assume the number

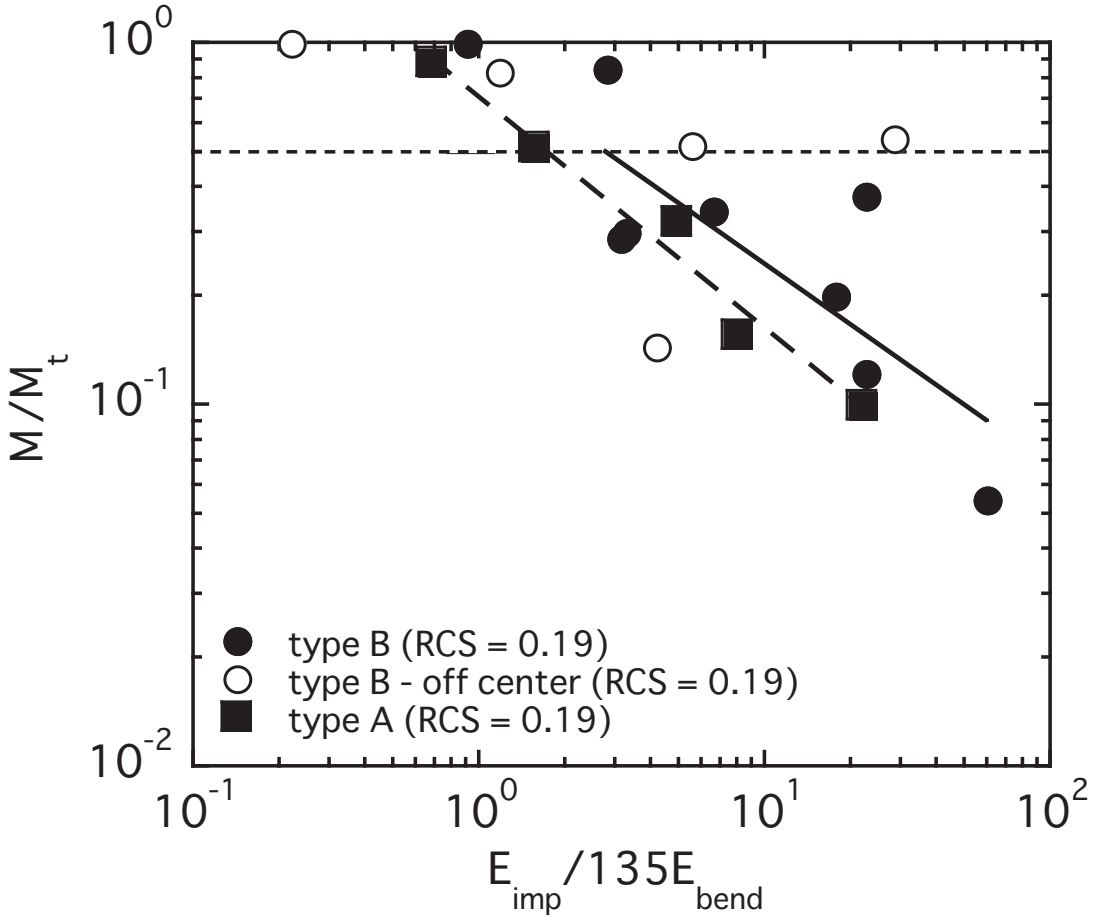

Figure 2.10: Normalized largest fragment mass versus normalized collisional energy for the weaker agglomerates (filled circle: central shot and smaller off-center shot) and the stronger agglomerates (filled square). The solid line is a fit to the weaker agglomerate data except for the large off-center impact (open circle) and data with M_l/M_t=1. The dashed line is a fit to the stronger agglomerate data.

of necks per particle is three, which is the minimum number we found for the agglomerates in this study. The minimum total number of necks n_{neck} is 135. The catastrophic disruption occurs, i.e., the largest mass fraction becomes smaller than 0.5, when $E_{imp} \sim$ a few times of $n_{neck} \times E_{bend}$. This is again similar to but somewhat smaller than what was shown for the disruption threshold for microscopic Ballistic cluster-cluster aggregation (BCCA) dust clusters bounded by van der Waals 'force (Wada *et al.*, 2009). The catastrophic disruption threshold of the clusters is shown to be about 10 times of the (number of particles) $\times$ (E_{break}), where E_{break} is the energy required for breaking one contact.

For oblique incidence and target shape effects on impacts, the results were summarized in Table 2.6. They are compared with the result of head-on impacts in Figure 2.11. No effect of target shape was

Table 2.6: Summary of oblique and edge-on collisions

Sample name	Target type	collision type	Projectile type	Projectile mass (g)	Projectile size (mm)	Impact velocity (m/s)	M_l/M_T
20110531	A	oblique	sphere	0.043	3.16	287	0.521
20110607	A	edge-on	sphere	0.043	3.16	290	0.126
20110609	A	edge-on	sphere	0.043	3.16	256	0.256
20110613	A	oblique	sphere	0.043	3.16	266	0.090
20110615	A	edge-on	sphere	0.030	2.82[*1]	95	0.390
20110622	A	oblique	sphere	0.030	2.89[*1]	125	0.122
20110629	A	oblique	sphere	0.031	2.79	>20[*2]	0.977
20110704	A	edge-on	sphere	0.033	2.91	<71[*2]	1

[*1] Estimated m_p mass.
[*2] Trigger failed. Impact velocity was estimated from the movie.

observed. The results also indicate no clear dependence of the results on impact angle, however the data is few and further investigation is required.

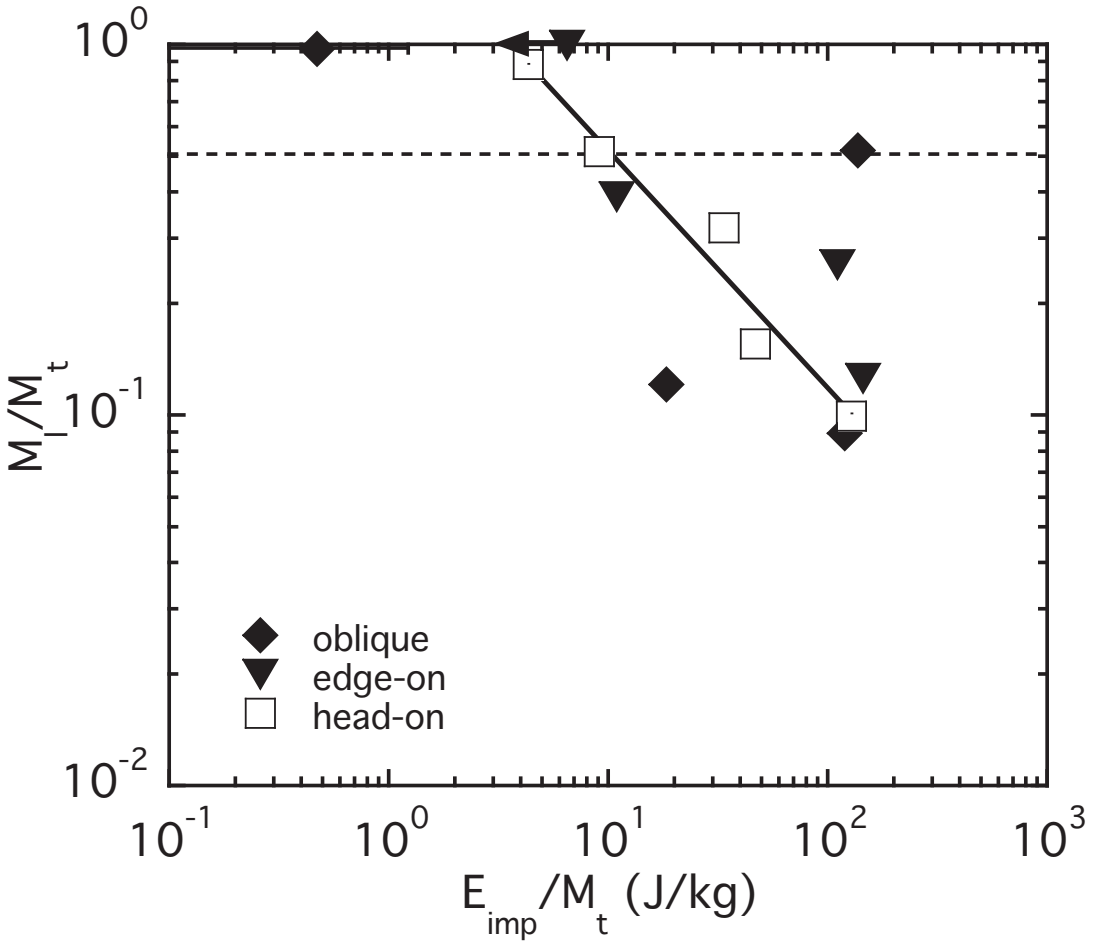

Figure 2.11: All plots are type A targets. Filled diamonds indicate oblique impacts which declined 45-degree to trajectory. Filled reversed triangles indicate impacts on side surface of cylindrical targets. Open squares indicate head-on collision.

2.4 Summary

In order to investigate the impact strength of porous bodies with different internal structures, especially those of sintered agglomerates, we performed strength measurements for sintered dimers and agglomerates of glass particles of about 5 mm in diameter. Sintering was conducted at three different temperatures with various heating durations. The critical tensile force to break a neck is proportional to the square of the neck radius only when the neck radius is much larger than the surface roughness, ~ 0.4 mm for the dimers of the rough particles. The critical bending force to break a neck is proportional to 3.0 ± 0.2 power of the neck radius and smaller than the critical tensile force.

We fabricated sintered glass agglomerates consisting of 90 particles. The agglomerate has a relative component size to the agglomerate size (RCS) of 0.19, that is ~ 100 times larger than the previous sintered glass beads targets used in impact disruption experiments. We determined the bulk static tensile strength of the agglomerates by Brazilian disc test and found that the results are consistent with the measurement values for the dimers.

Impact disruption experiments with velocity from 40 to 280 m/s were performed for the agglomerates with $\sim$ 40 % porosity of two different bulk tensile strengths. The energy densities required to catastrophically break-up the agglomerates with those of RCS = 0.19 less than those of previously investigated sintered glass, pure-ice, and ice-silicate mixture targets with similar porosity but of the smaller RCS values. On the other hand, the energy density required to catastrophically break-up the agglomerates with RCS of 0.027 is almost the same value as the previous works. This is probably due to much smaller number of necks of the target of RCS = 0.19 for the stress wave to travel through the agglomerates and much larger fraction of the surface particles which enables the particles to move more freely and thus be broken more easily. Such a dependence of impact disruption threshold on the number of constituent particles was shown for microscopic BPCA dust clusters bounded by van der Waal 's force (Wada *et al.*, 2009). We also found that the catastrophic disruption occurs when $E_{imp} \sim$ a few times of $n_{neck} \times E_{bend}$.

Present result implies that icy sintered agglomerates with larger RCS values, for example, finer pieces of fragments from sintered agglomerates such as comets or small icy moons, may have smaller Q_S^* value than other larger fragments with similar porosity and bulk tensile strength but much larger number of

constituent particles. This is opposite to the size-dependence of Q_S^* usually considered for the bodies in the strength regime (Holsapple *et al.*, 2002) and may affect collision cascade in debris discs (i.e., Kobayashi and Tanaka, 2010; Müller *et al.*, 2010). Finally, this study presents the critical tensile and bending forces to break a neck of sintered particles, the bulk tensile strength of sintered agglomerates, and impact strength of the agglomerates. Such information will be useful to validate numerical codes that model collisional disruption of agglomerates.

Chapter 3

Experimental Studies on the Formation Process of the Chondrite Parent Bodies

3.1 Introduction

Chondrites are composed of spherical objects called chondrules which are glassy and typically millimeter-sized and fine grains called matrix (Scott, 2002). Lots of works on chondrites have been performed for measurement of isotopic age, chemical composition, and so on. Especially for chondrules, it was found that they were molten under high temperature environment and rapidly cooled down (Jones *et al.*, 2000). By contrast, matrix consist of irregular shaped grains and some have not experienced high temperature (Brearley and Jones, 1998).

There are three major models for chondrule formation; x-wind model (Shu *et al.*, 2001), shock wave model (e. g., Hood and Horanyi, 1991; Yasuda *et al.*, 2009), and lightning model (e. g., Pilipp *et al.*, 1992; Güttler *et al.*, 2008). What is common for these models is that chondrules were formed uniformly, but at local place in protoplanetary disk.

Volume fraction of chondrules in chondrites is different for different chondrite types. For example, primitive CI chondrites include chondrules $<<$ 1 vol %, on the other hand, ordinary chondrites include them 60 to 80 vol % (Weisberg *et al.*, 2006). This indicates that the chondrule density in the protoplanetary disk varied along the heliocentric distance. Chondrite parent bodies are assigned to some classes of asteroids from comparison of their laboratory reflectance spectra with the observed reflectance spectra of asteroids. The fact that abundant classes of asteroids change with heliocentric distance as described in the following indicates that the chondrite parent bodies had some radial distribution. S-class asteroids, parent bodies of ordinary chondrites are found a lot at around 2 AU. C-class asteroids, parent bodies of carbonaceous chondrites are found a lot at around 3 AU (Mothé-Diniz *et al.*, 2003). Nakamura *et al.* (2011) analyzed surface particles of asteroid 25143 Itokawa which is classified as S-class asteroid and found that the mineralogy and mineral chemistry of them indicate thermally metamorphosed LL chondrites.

Chondrules formed around 200 to 300 million years after the formation age of Calcium Aluminum rich Inclusions (Kurahashi *et al.*, 2008). On the other hand, it takes only 10^3 years for dust aggregates to grow to typicall size of a few cm in diameter from dust particles of sub-micron size (Nomura and Nakagawa, 2006). Therefore, at the stage of the chondrule formation, dust size is expected at least a few cm.

In this work, we assume that chondrules and matrix were formed at different places in the protoplanetary

disk and subsequently they collided each other. We investigated the threshold velocity for a chondrule being embedded into matrix and the minimum size for matrix to capture a chondrule.

3.2 Experiments

We used polydisperse spherical silica particles of 0.8 ± 0.3 micron diameter and of 2200 kg/m^3 in density as matrix analogs to make agglomerates. For the velocity range from 0.2 to 2 m/s, we used the drop tube installed at TU Braunschweig in Germany (Beitz *et al.*, 2011). For the velocity range from 2 to 5 m/s, a spring gun developed for this study was used. A toy sling was also used at $\sim$ 1.5 m/s. For the velocity range from 20 to 300 m/s, a gas-gun installed at Kobe University was used (Setoh *et al.*, 2010).

3.2.1 Impact experiments at low velocity

Agglomerates of $\sim$ 50, $\sim$ 75, and $>$ 90 % in porosity were prepared for the collision experiments at lower impact velocity which were performed at TU Braunschweig. Compacted agglomerates of $\sim$ 50 % in porosity were prepared by pouring particles into a target container of 3 cm in diameter and 3 cm in depth pressing them strongly by hand. Medium agglomerates of $\sim$ 75 % in porosity were prepared by pouring aggregates of 68 % porosity into a target container of 3 cm in diameter. The determination of the porosity of the component dust aggregates was conducted by the same technique as Weidling *et al.* (2011). A component aggregate was put on a rotating stage and was taken images during it was rotated 360 degree. The diameter of the aggregate was measured for each horizontal pixel in the image sequence. The volume of each horizontal slice was calculated by determining the largest and the smallest diameter with assuming an elliptic shape. The volume was then calculated by integrating the areas of the slices. We used sieves of 1.0 and 1.6 mm mesh size to form these aggregates. Fluffy agglomerates of $>$ 90 % in porosity were prepared using random deposition apparatus (Blum *et al.*, 2006).

The projectiles used in this experiment were of 1 and 4.7 mm in diameter. Collisions under microgravity were performed by releasing both target and projectile at slightly different timing using a two-level release-mechanism. The dust target inside the plastic container was set on a plate of the lower release-mechanism which was mounted to a rotary solenoid. The projectile was suspended on a string, supported by a linear solenoid of the upper release-mechanism. By adjusting the release height of the projectile and the timings for dropping the projectile and the target, the relative impact velocities between the projectiles and the targets were set to 1-2 m/s and 10-20 cm/s, respectively. A high-speed camera was synchronously dropped

Table 3.1: Experiment conditions at low velocity

sample name	porosity (%)	projectile mass (g)	impact velocity (m/s)	result
110127-2	75	0.15	0.11	bounced
110127-3	49	0.15	0.17	bounced
110202-2	71	0.15	1.40	bounced
110202-3	72	0.15	1.43	bounced
110203-5	49	0.15	1.42	bounced
110203-2	72	0.0016	1.31	bounced
110203-1	72	0.0016	-	failed
110204-6	49	0.15	0.23	bounced
110204-3	73	0.15	0.23	nearly sticking
110209-2	73	0.15	0.26	nearly sticking
110209-1	73	0.15	0.31	nearly sticking
110209-4	50	0.15	0.12	bounced
110209-5	48	0.15	0.29	bounced
110210	> 90	0.0016	0.21	intrusion
110211	92	0.0016	1.31	intrusion

outside the glass tube and operated at a frame rate of 10 ms/frame. The experiment conditions are shown in Table 3.1.

3.2.2 Impact experiments at medium velocity

Agglomerates of about 3 cm in diameter, about 7.5 cm in length and 75 % in porosity were prepared for the collision experiment at medium velocity, $\sim$ 3 m/s using a spring gun. A toy sling was used at $\sim$ 1.5 m/s. Powder was poured into a container of 3 cm in diameter and $\sim$ 10 cm in length. A stainless rod of 450 g was put on the top of it to compress the powders to have the porosity of about 75 %.

The projectile trajectory was vertical to gravity. A projectile of $\sim$ 3 mm in diameter was put into a small cylindrical hole at top of the spring gun. By adjusting the length of the spring before the release, impact velocity could be changed from $\sim$ 2 to 5 m/s. The impact process was observed by a high-speed camera (Photoron FASTCAM SA1.1) which was operated at 100 μs/frame. The experiment conditions are shown in Table 3.2.

Table 3.2: Experiment conditions at medium velocity

sample name	porosity (%)	projectile mass (g)	impact velocity (m/s)	intrusion depth (mm)	result
20110720-2	75	0.029	1.35		bounced
20110720-3	75	0.030	1.94	-[*1]	intrusion
20110720-4	75	0.030	1.44		bounced
20110720-5	75	0.031	1.94		bounced
20111128-1	75	0.032	5.21	7.4	intrusion
20111128-2	74	0.033	-		nearly sticking[*2,3]
20111128-3	74	0.031	3.93	6.8	intrusion
20111128-4	75	0.030	2.51		bounced
20111128-5	75	0.028	3.55	6.2	intrusion
20111130-1	75	0.030	2.47	1.4	nearly sticking[*3]
20111130-2	75	0.036	3.30	7.5	intrusion
20111130-3	74	0.029	2.49		bounced
20111130-4	75	0.030	3.06	6.2	intrusion
20111130-5	75	0.030	3.03	7.2	intrusion

[*1] No data.
[*2] projectile fell down after stick to the target.
[*3] Intrusion depth is smaller than a projectile diameter.

3.2.3 Impact experiments at high velocity

Agglomerates of two porosities, ∼50, and ∼75 %, were prepared for the impact experiments at higher impact velocities at Kobe University. Compacted agglomerates of ∼ 50 % in porosity were prepared by pouring particles into a container and pressing it with a stainless rod by hand. Medium agglomerates of ∼ 75 % in porosity were prepared similarly to those in the medium velocity experiments described in the above.

The projectile trajectory was vertical to gravity. The projectile used in this experiment was glass bead of ∼ 3 mm in diameter. Impact velocities were determined with the images taken by a high-speed camera (Shimazu HPV-2) which was operated at frame rate of 16, 32, and 64 µs/frame. The experiment conditions are shown in Table 3.3.

3.2.4 Measurements of physical property of dust aggregate

Static compression tests of the aggregate of silica particles were performed to investigate their physical properties. Applied pressure to the aggregate was measured using a compression testing machine (Shi-

Table 3.3: Experiment conditions at higher velocity

sample name	porosity (%)	projectile mass (g)	impact velocity (m/s)	intrusion depth (mm)	result
081027-1	71	0.0016	91.5	[1]	intrusion
081028-1	71	0.0016	92.0	[1]	intrusion
081028-2	72	0.0016	164.3	[1]	intrusion
081028-3	71	0.0016	29.3	[1]	intrusion
081029-2	72	0.043	299.7	[1]	intrusion
081029-3	72	0.043	296.3	[1]	intrusion
081029-4	72	0.043	296.7	[1]	intrusion
081029-5	62	0.043	271.0	[1]	intrusion
081030-1	71	0.043	271.0	[1]	intrusion
081030-2	72	0.043	63.9	[1]	intrusion
081030-3	72	0.0016	76.2	[1]	intrusion
081030-4	73	0.0016	154.0	[1]	intrusion
20110714-1	73	0.028	50.9	[1]	intrusion
20110714-2	73	0.032	32.5	[1]	intrusion
20110714-3	73	0.032	-	[1]	intrusion
20110714-4	76	0.029	-	[1]	intrusion
20110714-5	76	0.032	55.4	[1]	intrusion
20110719-1	75	0.032	35.8	[1]	intrusion
20110719-2	75	0.032	35.3	28.7	intrusion
20110719-3	74	0.034	39.4	31.7	intrusion
20110719-4	75	0.034	45.9	[1]	intrusion
20110719-5	75	0.038	31.7	26.9	intrusion
20110720-1	75	0.034	37.2	30.8	intrusion
20111003-1	51	0.030	89.0	9.5	intrusion
20111003-2	49	0.032	56.5	4.8	intrusion
20111003-3	50	0.031	32.4		bounced
20111003-4	49	0.030	46.9	4.0	intrusion
20111003-5	47	0.034	19.1		bounced

[1] No data

mazu EZ Graph).

Static compression tests were performed using containers of 5, 10, 15 and 20 mm in diameter. Applied force was up to 9.8 kN and the nominal loading rate was 0.01 mm/s. The height of the top surface of the particles was about 3 mm after the measurement.

Pellets of 5 mm in diameter and about 3 mm in height were formed to measure the uni-axial compressive strength of compressed dust agglomerates. Porosity of the pellets were 42 and 46 %, respectively. The samples were fixed on the stage of a compression testing machine and applied force perpendicular to the upper base of the cylindrical pellet.

3.3 Results of dust impact experiments

3.3.1 Results of impact experiment

Three different outcomes were observed, intrusion, bouncing and (nearly) sticking as shown in Figure 3.1. Figure 3.2 indicates the relation between collisional outcome and porosity and impact velocity. Nearly sticking (filled triangle) means that the displacement of the projectile could not be confirmed more than 120 ms after the collision for low velocity experiments and that the intrusion depth is smaller than the projectile diameter for medium velocity experiments. There were two nearly sticking in medium velocity experiments. For one of them, the projectile fell down after collision-sticking due to gravity. Open diamond represents the boundary between bouncing and sticking for monodisperse dust agglomerates of 85 % in porosity (Blum and Wurm, 2008). For the targets of $\sim$ 50 and $\sim$ 75 % in porosity, intrusion occurred at higher velocity and bouncing occurred at lower velocity. At $v < 2$ m/s, projectile could intrude into target only when a target had higher porosity.

Intrusion depth is measured after collision as shown in Figure 3.3. The value of the depth is the sum of the intruded space measured by a caliper and the projectile diameter. For the targets of $\sim$ 50 % in porosity, intrusion started at 46 m/s and the depth increases with increase in impact velocity. For the targets of $\sim$ 75 % in porosity, intrusion occurred at $\sim$ 3 m/s. Dashed lines indicate the intrusion depth when the drag is proportional to the strength of target. Solid line indicates the intrusion depth when the drag is proportional to the square of impact velocity. For both types of targets, the data is consistent with the dashed lines at lower impact velocities. The data is consistent with the solid line for the target of 75 % in porosity at high velocities.

3.3.2 Results of measurement of physical properties of dust

Figure 3.4 shows the compression curves for all types of container. These curves are almost similar except for the curve of the container with 5 mm in diameter. Focused on the elastic regime of the dust agglomerate, the pressure of elastic limit, that is triaxial compressive strength was determined as shown in Figure 3.5. The point that slope changed indicates the elastic limit pressure of the dust. The target shown in Figure 3.5 had initially 56 % in porosity. In Figure 3.6 filled circles show the pressure of the elastic limit

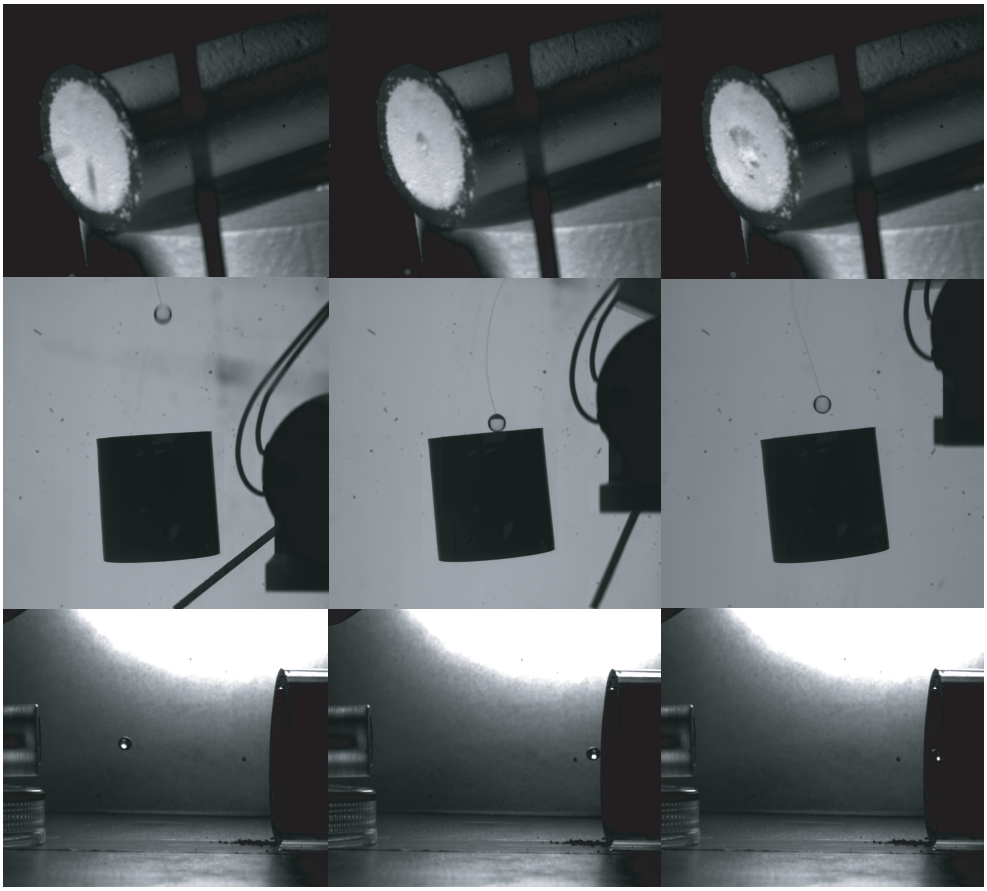

Figure 3.1: Upper image sequence is an example for intrusion (20110719-3). The projectile is colliding with the target in left image. After 0.32 ms from the left image, the projectile collided with the target in middle image. After 3.2 ms from the collision, the projectile was already intruded into the target in right image. Middle image sequence is an example for bouncing (20110203-5). Left image is before collision. Time interval between the images is 2.1 ms and 1.5 ms, respectively. Bottom image sequence is an example for sticking (20111130-1). Time interval between the images is 13 ms and 2 ms, respectively.

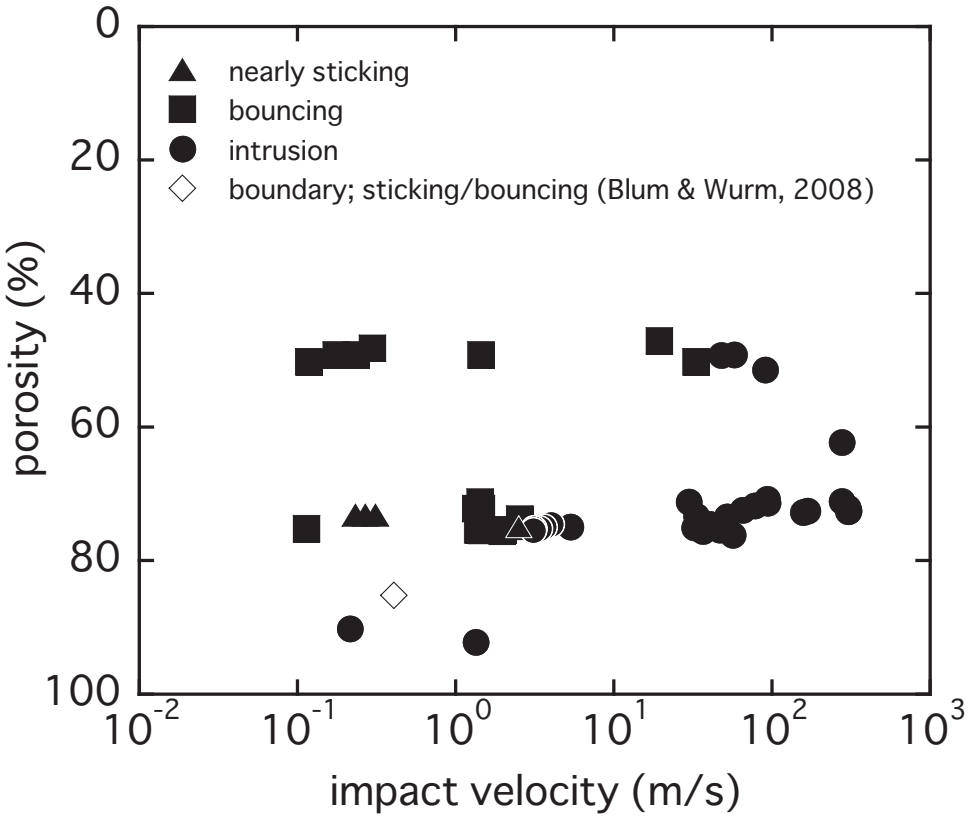

Figure 3.2: Filled circles represent experiments in which the projectile was embedded, for the filled squares, the projectile bounced off from the target. Filled triangles denote cases in which the chondrule nearly stick to the target.

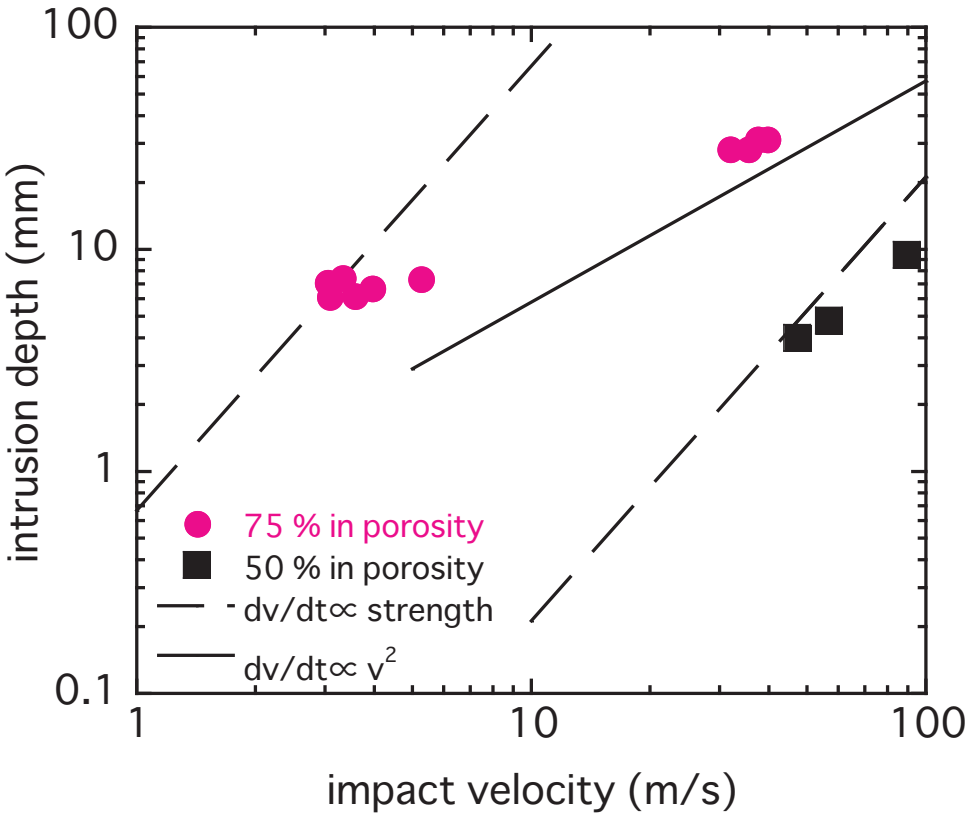

Figure 3.3: Circles represent the data for the targets of $\sim$ 75 % in porosity. Intrusion starts to occur at $\sim$ 3 m/s. Squares represent the data for the targets of $\sim$ 50 % in porosity. Intrusion occurred at 46 m/s. Dashed lines indicate the drag is proportional to the strength of target. Solid line indicates the drag is proportional to the square of impact velocity.

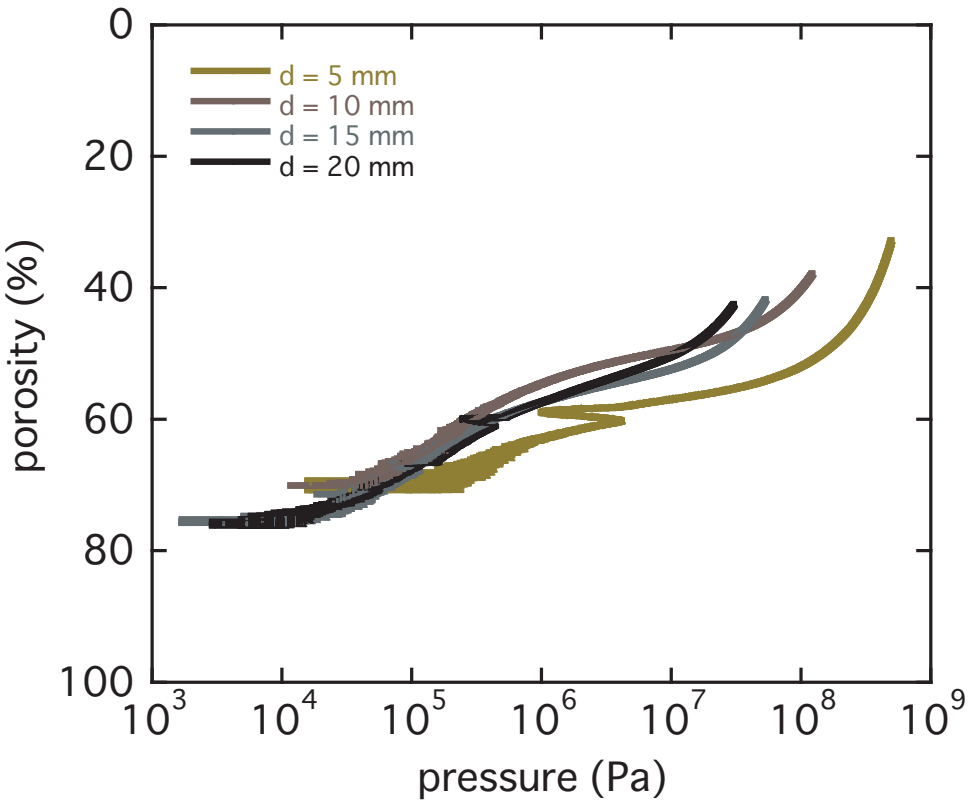

Figure 3.4: Compression curves measured for the container of 5, 10, 15 and 20 mm in diameter are indicated gradation color.

and open circles show the compressive strength of pellet shaped dust agglomerate with porosities of 42 and 46 % by uniaxial compressive test. Gray curves are the compression curves of dust agglomerates with the containers of 15 mm in diameter. There is porosity distribution at a pressure for each measurement being independent of amount of powder. The uniaxial compressive strength is lower than the necessary pressure for compressing the dust in the container, which is consistent with the fact that uniaxial compressive strength is lower than triaxial comressive strength (Güttler *et al.*, 2009). Compressive strengths of the dust are consistent with the pressure at the same porosity on the compression curve within error bar. We thus consider that the any point on the compression curve represents the compressive strength of the agglomerate of that porosity.

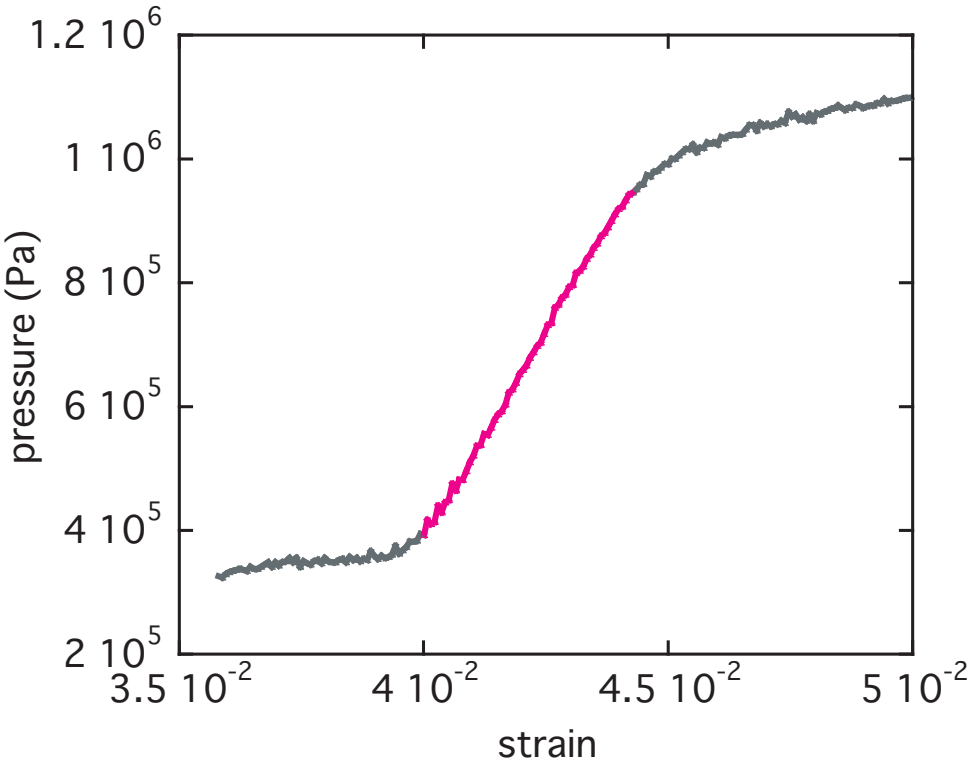

Figure 3.5: Compression curve for the dust agglomerate of 56 % in porosity. The point that the slope changed indicates the compressive strength of the agglomerate (Y_c).

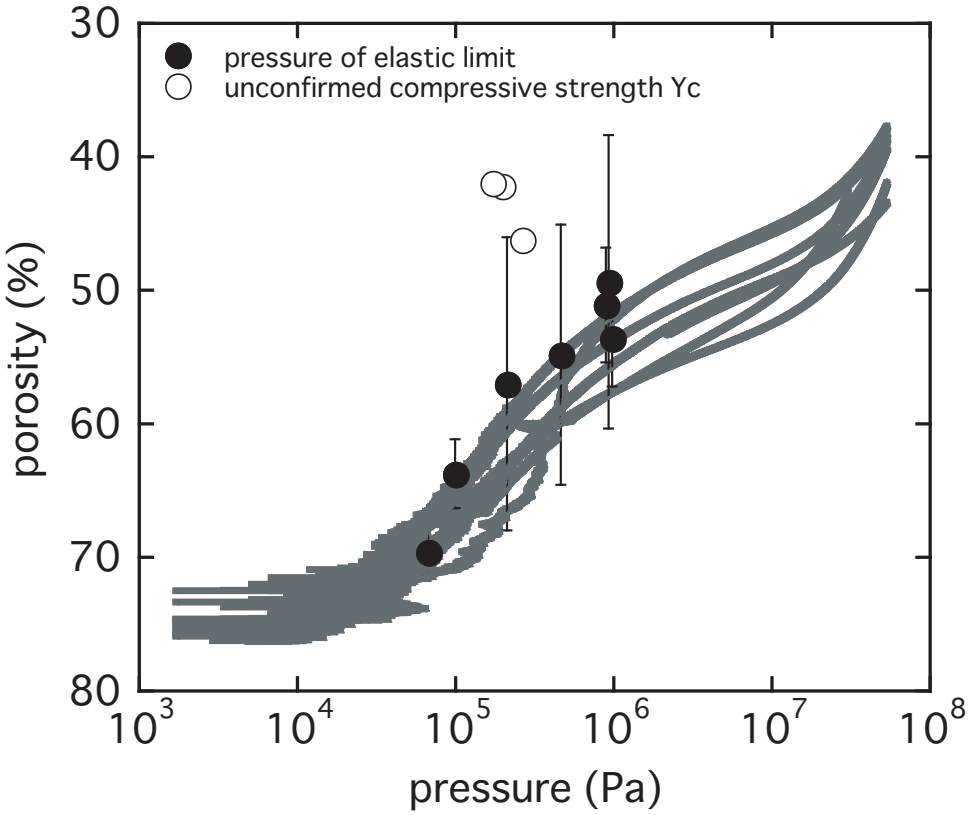

Figure 3.6: Gray curves represent compression curves for individual dust agglomerates with container of 15 mm in diameter. Filled circles represent the pressure of elastic limit of dust agglomerates, that is triaxial compressive strength. Open circles represent the unconfined uniaxial compressive strength Y_c of the pellet shaped dust agglomerates.

3.4 Discussion

3.4.1 The boundary between intrusion and bouncing

In order to discuss the conditions for bouncing and intrusion, we convert the impact velocity in Fig. 3.2 into pressure in the target at impact, and compare it with the static strength of the target. When a projectile collides to a target at low velocity, impact pressure is given by the following equation (Appendix)

$$P = \rho C v \tag{3.1}$$

where, ρ, C, and v denote bulk density of the target, sound velocity of the target, and impact velocity, respectively.

The sound velocity of the target is estimated by the following equation,

$$C = \left(\frac{\text{slope of elastic portion of the compression curve}}{\text{bulk density}} \right)^{0.5} \tag{3.2}$$

The sound velocity of 77 % porosity dust agglomerate was determined with the value of the slope and the bulk density at the maximum pressure shown in Fig. 3.5.

The sound velocities of individual dust agglomerate were determined by the eq. 3.1 as shown in Figure 3.7. The empirical equation for sound velocity of dust agglomerate were obtained as

$$C = a e^{b(1-\phi)} \tag{3.3}$$

where, a = 3.9 $\pm$ 2.5 $\times$ 10^5, b = -0.14 $\pm$ 0.01 and $1-\phi$ denotes bulk porosity of dust agglomerate. The sound velocity for the collision experiments were calculated by the eq. 3.3.

The collisional outcomes are shown in Figure 3.8 with converted pressure. Intrusion of projectile indeed occurs if impact pressure is larger than the target compressive strength.

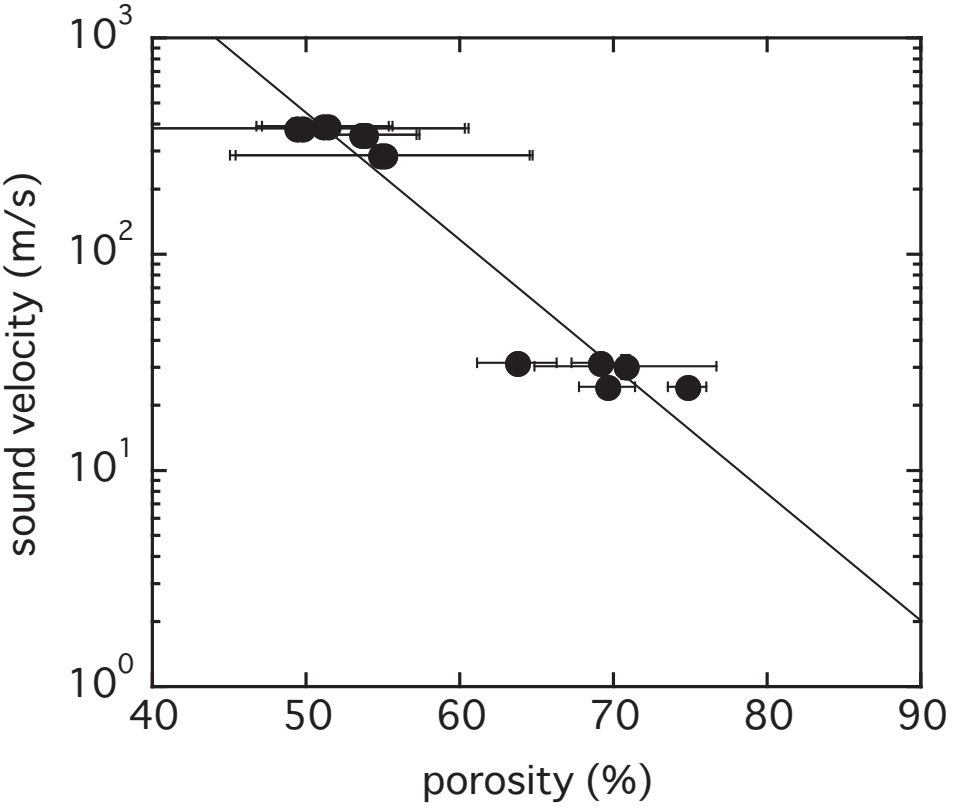

Figure 3.7: Filled circles indicate the sound velocities for the dust agglomerates derived from the eq. 3.2. Solid line is fitting line represented as the eq. 3.3.

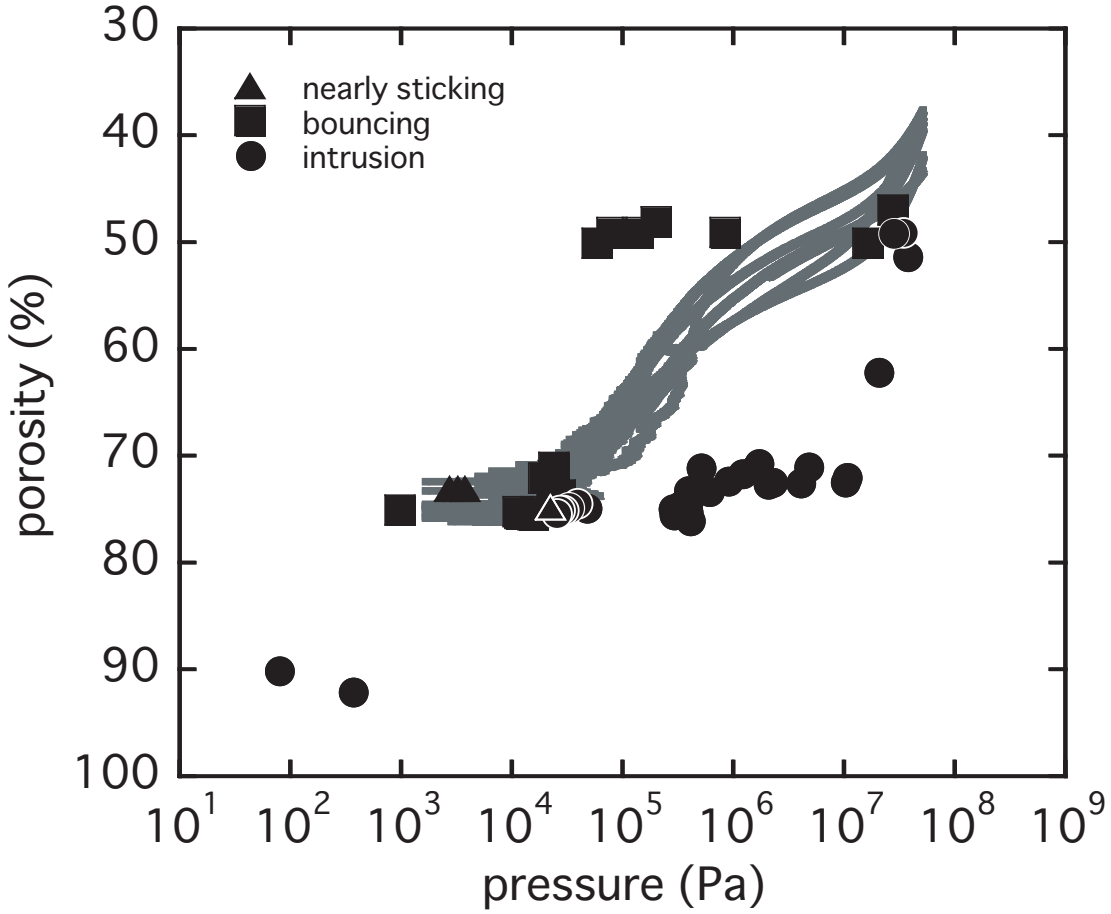

Figure 3.8: Impact velocity in Figure 3.2 is converted into impact pressure indicated as filled square. Gray curves are compression curves of dust agglomerates.

3.4.2 Implication for chondule-matrix collision in protoplanetary disk

From the results of the minimum intrusion velocity, appropriate dust sizes in protoplanetary disk were estimated using the model of Weidenschilling and Cuzzi (1993). Dust agglomerates of $\sim$ 50 % porosity should collide with velocity larger than 50 m/s to capture a chondrule. A 3 mm dust has relative velocity of 50 m/s with dust of 90 cm. Dust agglomerate of $\sim$ 75 % porosity has relative velocity 3 m/s to capture a chondlure. A 3 mm dust has relative velocity of 3 m/s with dust of 10 cm. These estimated matrix sizes are large enough to stop the chondrule according to the intrusion depth shown in Figure 3.3.

3.5 Summary

In order to investigate the conditions under which chodrules can be embedded into matrix, collision experiments were performed using glass beads of 1, about 3 and 4.7 mm diameter as chondrule analog and polydisperse dust agglomerate of 0.8 ± 0.3 μm diameter as matrix analog at impact velocity from 0.2 to 300 m/s.

Intrusion occurred at higher impact velocities and for the targets with higher porosity. To obtain impact pressure for the targets, the sound velocity of the target was estimated by the slope of elastic part of the compression curve of aggregates. From the data of the elastic limit of the dust agglomerates, the empirical equation for the sound velocity was obtained. The sound velocities of the targets performed the collision experiments were derived from the empirical equation, which are 460, 15 and 2 m/s for 50, 75 and 90 % porosity targets, respectively. As the result, we found the condition of intrusion-bouncing boundary. Bouncing occurs when the compressive strength of the target is larger than the impact pressure. Meanwhile intrusion occurs when the compressive strength of the target is smaller than the impact pressure. Appropriate dust size colliding with dust of 3 mm in diameter was 90 and 10 cm in diameter at the minimum intrusion velocities in the standard model of protoplanetary disk. The sizes are enough larger than the intrusion depth and they are likely to capture a chondrule.

Chapter 4

General summary

Porous bodies in the solar system have variety of internal structure. Examples are a porous structure consisting of pile of components connecting together by smaller cohesion than the strength of the components themselves and a structure consisting of voids generated by evaporation of volatile elements. In this study, I focused on the porous bodies consists of pile of components with weaker bulk strength than component strength.

In Chapter 2, I investigated porous structure consisting of components connected by physical necks developed by sintering process. The effect of the size ratio of the component to the target on the impact disruption threshold (Q_s^*) was examined. Impact disruption experiments were performed using glass bead of 3 mm in diameter and cylindrical polycarbonate of 3 mm in diameter and 6 mm in length as projectiles and agglomerates with three different physical properties. The bulk tensile strength and the RCS values of the targets are $3.53 \pm 0.87 \times 10^5$ Pa and $7.4 \pm 1.5 \times 10^5$ Pa for RCS of 0.19 and $2.9 \pm 1.54 \times 10^5$ for RCS of 0.027, respectively. For the targets of RCS of 0.19, Q_s^* is smaller than the previous works (Arakawa *et al.*, 2002; Arakawa and Tomizuka, 2004; Setoh *et al.*, 2010) of targets with RCS of 10^{-3} with the similar bulk tensile strength. On the other hand, we showed the targets of RCS 0.027 have the Q_s^* value similar to those of targets of RCS 10^{-3}. If a target consists of small number of particles (i.e., those with larger RCS values), stress wave meets less number of necks and therefore can transmit more energy through out the target. Also, the larger fraction of the surface particles enables the particles to move more freely and thus can be broken more easily. The result implies that Q_s^* of icy porous bodies is likely to

change depending on RCS if their body was sintered.

In Chapter 3, I investigated porous structure consisting of components connected only by cohesion of fine particles in order to examine the possibility of the formation of chondrite parent bodies. Collisional experiments were performed using glass bead of 1, 3 and 4.7 mm in diameter as projectiles and agglomerates of three different porosities: 50, 75 and 90 %, which consist of silica particle of 0.8 ± 0.3 mm in diameter as targets. The velocity threshold between projectile's intrusion and bouncing was determined by varying impact velocities from 0.2 to $\sim$ 300 m/s using three types of accelerators. There were three types of collisional outcomes; bouncing, (nearly) sticking and intrusion of the projectile. The impact pressure at the threshold velocity of intrusion was estimated using target density, sound velocity and the impact velocity and compared with the compressive strength of the targets. The sound velocities of the targets were derived from the slope of compression curve within the elastic limit and were 460, 15 and 2 m/s for 50, 75 and 90 % porosity targets. The compression curves of silica dust agglomerates in a stainless cylindrical container were measured. We assumed the compression curve shows the value of the target bulk strength at any given porosity. The collision results were thus compared with the targets bulk strength. We found that the threshold of bouncing-intrusion depends on the relation between the compressive strength of the target and the impact pressure. The projectile was embedded at the impact velocities lower than 2 m/s in case of the 90 % porosity targets. The projectile intruded the target at velocities larger than 3 m/s in the targets of $\sim$ 75 % in porosity. The projectile began to intrude the target at 46 m/s in the target of $\sim$ 50 % in porosity. The intrusion depth for the targets of 50 and 75 % in porosity was measured and increased with impact velosity. According to a model on relative velocity between dusts of different sizes in a protoplanetary disk (Weidenschilling and Cuzzi, 1993), the dusts having velocity large enough to capture a 3 mm chondrule have size also large enough to stop the chondrule.

It was found that the bodies which has the same static bulk strength may have different Q_s^* depending on the internal structure such as RCS. Whether the collision outcome is intrusion or bouncing can be estimated by a comparison of the bulk strength of the target and the impact pressure.

Acknowledgments

I would like to thank A. M. Nakamura for helpful suggestions and discussions in this paper. I also acknowledge M. Arakawa, Y. Otofuji, A. Tsuchiyama, P. Michel, H. Kimura, A. Suzuki, M. Yasui and all colleages in the laboratory for helpful discussions. K. Tomeoka and Y. Seto gave insightful comments and suggestions.

Discussions with T. Kadono and H. Tanaka, K. Wada, S. Okuzumi, H. Kobayashi, T. Tanigawa have been illuminating. I received generous support and useful discussion from J. Blum, C. Güttler and R. Schräpler, and D. Heisselmann, E. Beitz, R. Weidling, S. Kothe, and D. Beger.

I have had the support and encouragement of S. Hasegawa, T. Morota, Y. Sekine, A. Yoshihara K. Okudaira, K. Kitazato and C. Honda.

Appendix

The eq. 3.1 in chapter 3.4 is derived from the following equations. Impact pressure for projectile and target are given by the eq. 1.10 in chapter 1 if $u_p << C$,

$$P_t = \rho_t C_t u_t \tag{4.1}$$

$$P_i = \rho_i C_i u_i \tag{4.2}$$

where the subscript $_t$ and $_i$ indicate target and impactor, respectively.

The impact pressure at the moment of impact,

$$P_t = P_i. \tag{4.3}$$

By substituting the eq. 4.1 and 4.2 into the eq. above, we obtain the following

$$\rho_t C_t u_t = \rho_i C_i u_i. \tag{4.4}$$

The relation between impact velocity and particle velocity is $v = u_t + u_i$. Then u_i is represented as

$$u_i = v - u_t. \tag{4.5}$$

u_t is obtained by substituting the eq. 4.5 into the eq. 4.4

$$u_t = \frac{\rho_i C_i}{\rho_t C_t + \rho_i C_i} v. \tag{4.6}$$

Substituting the eq. 4.6 into the eq. 4.1 gives P_t as

$$P_t = \rho_t C_t \frac{\rho_i C_i}{\rho_t C_t + \rho_i C_i} v \tag{4.7}$$

when $C_t \ll C_i$, $\rho_t \ll \rho_i$, P_t is represented as follow

$$P_t = \rho_t C_t v. \tag{4.8}$$

Bibliography

Arakawa, M., J. Leliwa-Kopystynski, and N. Maeno 2002. Impact Experiments on Porous Icy-Silicate Cylindrical Blocks and the Implication for Disruption and Accumulation of Small Icy Bodies. *Icarus* **158**, 516–531.

Arakawa, M., and D. Tomizuka 2004. Ice-silicate fractionation among icy bodies due to the difference of impact strength between ice and ice-silicate mixture. *Icarus* **170**, 193–201.

Asphaug, E., E. V. Ryan, and M. T. Zuber 2002. *Asteroid Interiors*, pp. 463–484.

Beitz, E., C. Güttler, J. Blum, T. Meisner, J. Teiser, and G. Wurm 2011. Low-velocity Collisions of Centimeter-sized Dust Aggregates. *The Astrophysical Journal* **736**, 34.

Blum, J., R. Schräpler, B. J. R. Davidsson, and J. M. Trigo-Rodríguez 2006. The Physics of Protoplanetesimal Dust Agglomerates. I. Mechanical Properties and Relations to Primitive Bodies in the Solar System. *The Astrophysical Journal* **652**, 1768–1781.

Brearley, A. J., and R. H. Jones 1998. *Chondritic Meteorites*, pp. 3:1–3:398. Planetary Meteorites. Mineralogical Society of America.

Britt, D. T., D. Yeomans, K. Housen, and G. Consolmagno 2002. *Asteroid Density, Porosity, and Structure*, pp. 485–500. Asteroids III. Univ. of Arizona Press, Tucson.

Charnoz, S., A. Morbidelli, L. Dones, and J. Salmon 2009. Did Saturn's rings form during the Late Heavy Bombardment? *Icarus* **199**, 413–428.

Cintala, M. J., L. Berthoud, and F. Hörz 1999. Ejection-velocity distributions from impacts into coarse-grained sand. *Meteoritics and Planetary Science* **34**, 605–623.

Davis, D. R., C. R. Chapman, R. Greenberg, S. J. Weidenschilling, and A. W. Harris 1979. *Collisional evolution of asteroids - Populations, rotations, and velocities*, pp. 528–557.

Durham, W. B., W. B. McKinnon, and L. A. Stern 2005. Cold compaction of water ice. *Geophysical Research Letters* **32**, 18202–+.

Farinella, P., and D. R. Davis 1996. Short-Period Comets: Primordial Bodies or Collisional Fragments? *Science* **273**, 938–941.

Fujiwara, A. 1980. On the mechanism of catastrophic destruction of minor planets by high-velocity impact. *Icarus* **41**, 356–364.

Fujiwara, A., G. Kamimoto, and A. Tsukamoto 1977. Destruction of basaltic bodies by high-velocity impact. *Icarus* **31**, 277–288.

Fujiwara, A., J. Kawaguchi, D. K. Yeomans, M. Abe, T. Mukai, T. Okada, J. Saito, H. Yano, M. Yoshikawa, D. J. Scheeres, O. Barnouin-Jha, A. F. Cheng, H. Demura, R. W. Gaskell, N. Hirata, H. Ikeda, T. Kominato, H. Miyamoto, A. M. Nakamura, R. Nakamura, S. Sasaki, and K. Uesugi 2006. The Rubble-Pile Asteroid Itokawa as Observed by Hayabusa. *Science* **312**, 1330–1334.

Gault, D. E., F. Hörz, and J. B. Hartung 1972. Effects of microcratering on the lunar surface. In A. E. Metzger, J. I. Trombka, L. E. Peterson, R. C. Reedy, & J. R. Arnold (Ed.), *Lunar and Planetary Science Conference Proceedings*, Volume 3 of *Lunar and Planetary Science Conference Proceedings*, pp. 2713–+.

Gault, D. E., and J. A. Wedekind 1969. The destruction of tektites by micrometeoroid impact. *J. Geophys. Res.* **74**, 6780–6794.

Giblin, I., D. R. Davis, and E. V. Ryan 2004. On the collisional disruption of porous icy targets simulating Kuiper belt objects. *Icarus* **171**, 487–505.

Greenberg, R., and W. K. Hartmann 1977. Impact Strength: A Fundamental Parameter of Collisional Evolution. In *Bulletin of the American Astronomical Society*, Volume 9 of *Bulletin of the American Astronomical Society*, pp. 455–+.

Greenberg, R., W. K. Hartmann, C. R. Chapman, and J. F. Wacker 1978. Planetesimals to planets - Numerical simulation of collisional evolution. *Icarus* **35**, 1–26.

Güttler, C., M. Krause, R. J. Geretshauser, R. Speith, and J. Blum 2009. The Physics of Protoplanetesimal Dust Agglomerates. IV. Toward a Dynamical Collision Model. *The Astrophysical Journal* **701**, 130–141.

Güttler, C., T. Poppe, J. T. Wasson, and J. Blum 2008. Exposing metal and silicate charges to electrical discharges: Did chondrules form by nebular lightning? *Icarus* **195**, 504–510.

Hartmann, W. K. 1978. Planet formation - Mechanism of early growth. *Icarus* **33**, 50–61.

Hiraoka, K. 2008. *Experimental study of the impact cratering process in the strength regime*. Ph. D. thesis, Kobe University.

Hiraoka, K., M. Arakawa, M. Setoh, and A. M. Nakamura 2008. Measurements of target compressive and tensile strength for application to impact cratering on ice-silicate mixtures. *J. Geophys. Res. (Planets)* **113**, 2013.

Hirata, N., O. S. Barnouin-Jha, C. Honda, R. Nakamura, H. Miyamoto, S. Sasaki, H. Demura, A. M. Nakamura, T. Michikami, R. W. Gaskell, and J. Saito 2009. A survey of possible impact structures on 25143 Itokawa. *Icarus* **200**, 486–502.

Holsapple, K., I. Giblin, K. Housen, A. Nakamura, and E. Ryan 2002. *Asteroid Impacts: Laboratory Experiments and Scaling Laws*, pp. 443–462. Asteroids III. Univ. of Arizona Press, Tucson.

Holsapple, K. A. 1994. Catastrophic disruptions and cratering of solar system bodies: A review and new results. *Planetary and Space Science* **42**, 1067–1078.

Hood, L. L., and M. Horanyi 1991. Gas dynamic heating of chondrule precursor grains in the solar nebula. *Icarus* **93**, 259–269.

Housen, K. R., and K. A. Holsapple 1990. On the fragmentation of asteroids and planetary satellites. *Icarus* **84**, 226–253.

Housen, K. R., and K. A. Holsapple 1999. Scale Effects in Strength-Dominated Collisions of Rocky Asteroids. *Icarus* **142**, 21–33.

Jones, R. H., T. Lee, H. C. Connolly, Jr., S. G. Love, and H. Shang 2000. Formation of Chondrules and CAIs: Theory VS. Observation. *Protostars and Planets IV*, 927.

Kingery, W. D., and M. Berg 1955. Study of the Initial Stages of Singering, Solids by Viscous flow, Evaporation-Condensation, and Self Diffusion. *J. Appl. Phys.* **26**, 1205–1212.

Kobayashi, H., and H. Tanaka 2010. Fragmentation model dependence of collision cascades. *Icarus* **206**, 735–746.

Kurahashi, E., N. T. Kita, H. Nagahara, and Y. Morishita 2008. ^{26}Al ^{26}Mg systematics of chondrules in a primitive CO chondrite. *gca* **72**, 3865–3882.

Love, S. G., F. Hörz, and D. E. Brownlee 1993. Target Porosity Effects in Impact Cratering and Collisional Disruption. *Icarus* **105**, 216–224.

Machii, N., and A. M. Nakamura 2011. Experimental study on static and impact strength of sintered agglomerates. *Icarus* **211**, 885–893.

Melosh, H. J. 1989. *Impact cratering: A geologic process*.

Michikami, T., K. Moriguchi, S. Hasegawa, and A. Fujiwara 2007. Ejecta velocity distribution for impact cratering experiments on porous and low strength targets. *Planet. Space Sci.* **55**, 70–88.

Mothé-Diniz, T., J. M. Á. Carvano, and D. Lazzaro 2003. Distribution of taxonomic classes in the main belt of asteroids. *Icarus* **162**, 10–21.

Müller, S., T. Löhne, and A. V. Krivov 2010. The Debris Disk of Vega: A Steady-state Collisional Cascade, Naturally. *Astrophys J.* **708**, 1728–1747.

Nakamura, A. M., K. Hiraoka, Y. Yamashita, and N. Machii 2009. Collisional disruption experiments of porous targets. *Planet. Space Sci.* **57**, 111–118.

Nakamura, T., T. Noguchi, M. Tanaka, M. E. Zolensky, M. Kimura, A. Tsuchiyama, A. Nakato, T. Ogami, H. Ishida, M. Uesugi, T. Yada, K. Shirai, A. Fujimura, R. Okazaki, S. A. Sandford, Y. Ishibashi, M. Abe, T. Okada, M. Ueno, T. Mukai, M. Yoshikawa, and J. Kawaguchi 2011. Itokawa Dust Particles: A Direct Link Between S-Type Asteroids and Ordinary Chondrites. *Science* **333**, 1113–.

Nomura, H., and Y. Nakagawa 2006. Dust Size Growth and Settling in a Protoplanetary Disk. *The Astrophysical Journal* **640**, 1099–1109.

Pilipp, W., T. W. Hartquist, and G. E. Morfill 1992. Large electric fields in acoustic waves and the stimulation of lightning discharges. *The Astrophysical Journal* **387**, 364–371.

Poppe, T. 2003. Sintering of highly porous silica-particle samples: analogues of early Solar-System aggregates. *Icarus* **164**, 139–148.

Porco, C. C., P. C. Thomas, J. W. Weiss, and D. C. Richardson 2007. Saturn's Small Inner Satellites: Clues to Their Origins. *Science* **318**, 1602–1607.

Richardson, D. C., Z. M. Leinhardt, H. J. Melosh, W. F. Bottke, Jr., and E. Asphaug 2002. *Gravitational Aggregates: Evidence and Evolution*, pp. 501–515.

Ryan, E. V., D. R. Davis, and I. Giblin 1999. A Laboratory Impact Study of Simulated Edgeworth-Kuiper Belt Objects. *Icarus* **142**, 56–62.

Ryan, E. V., W. K. Hartmann, and D. R. Davis 1991. Impact experiments. III - Catastrophic fragmentation of aggregate targets and relation to asteroids. *Icarus* **94**, 283–298.

Ryan, E. V., and H. J. Melosh 1998. Impact Fragmentation: From the Laboratory to Asteroids. *Icarus* **133**, 1–24.

Scott, E. R. D. 2002. Meteorite Evidence for the Accretion and Collisional Evolution of Asteroids. *Asteroids III*, 697–709.

Setoh, M., A. M. Nakamura, P. Michel, K. Hiraoka, Y. Yamashita, S. Hasegawa, N. Onose, and K. Okudaira 2010. High- and low-velocity impact experiments on porous sintered glass bead targets of different compressive strengths: Outcome sensitivity and scaling. *Icarus* **205**, 702–711.

Sheppard, S. S., and D. C. Jewitt 2002. The shapes, densities, and phase functions of trans-Neptunian objects. In B. Warmbein (Ed.), *Asteroids, Comets, and Meteors: ACM 2002*, Volume 500 of *ESA Special Publication*, pp. 21–24.

Shu, F. H., H. Shang, M. Gounelle, A. E. Glassgold, and T. Lee 2001. The Origin of Chondrules and Refractory Inclusions in Chondritic Meteorites. *The Astrophysical Journal* **548**, 1029–1050.

Sirono, S. 1999. Effects by sintering on the energy dissipation efficiency in collisions of grain aggregates. *Astron. Astrophys.* **347**, 720–723.

Trilling, D. E., and G. M. Bernstein 2006. Light Curves of 20-100 km Kuiper Belt Objects Using the Hubble Space Telescope. *Astrophys J.* **131**, 1149–1162.

Wada, K., H. Tanaka, T. Suyama, H. Kimura, and T. Yamamoto 2009. Collisional Growth Conditions for Dust Aggregates. *Astrophys J.* **702**, 1490–1501.

Weidenschilling, S. J., and J. N. Cuzzi 1993. *Formation of planetesimals in the solar nebula*, pp. 1031–1060.

Weidling, R., C. Güttler, and J. Blum 2011. Free Collisions in a Microgravity Many-Particle Experiment. I. Dust Aggregate Sticking at Low Velocities. *ArXiv e-prints*.

Weisberg, M. K., T. J. McCoy, and A. N. Krot 2006. *Systematics and Evaluation of Meteorite Classification*, pp. 19–52.

Yasuda, S., H. Miura, and T. Nakamoto 2009. Compound chondrule formation in the shock-wave heating model: Three-dimensional hydrodynamics simulation of the disruption of a partially-molten dust particle. *Icarus* **204**, 303–315.